

VO₂ under hydrostatic pressure: Isostructural phase transition close to a critical end-point

P. Bouvier^{1*}, L. Bussmann¹, D. Machon^{2,3,4}, I. Breslavetz⁵, G. Garbarino⁶, P. Strobel¹, V. Dmitriev¹

¹ Université Grenoble Alpes, Institut Néel CNRS, 25 Rue des Martyrs, 38042, Grenoble, France.

² Laboratoire Nanotechnologies et Nanosystèmes (LN2) - CNRS UMI-3463 Institut Interdisciplinaire d'Innovation Technologique (3IT), Université de Sherbrooke, 3000 Boulevard Université, Sherbrooke, J1K OA5 Québec, Canada

³ Institut Interdisciplinaire d'Innovation Technologique (3IT), Université de Sherbrooke, 3000 Boulevard Université, Sherbrooke, J1K OA5 Québec, Canada

⁴ Université de Lyon, INSA Lyon, CNRS, Ecole Centrale de Lyon, Université Claude Bernard Lyon 1, CPE Lyon, INL, UMR5270, 69621 Villeurbanne, France

⁵ LNCMI, UPR 3228, CNRS, EMFL, Université Grenoble Alpes, 38000 Grenoble, France

⁶ European Synchrotron Radiation Facility, BP220, 38043 Grenoble Cedex, France.

* Corresponding author. E-mail address: pierre.bouvier@neel.cnrs.fr (P. Bouvier).

Abstract

The high-pressure behavior of monoclinic VO₂ is revisited by a combination of Raman spectroscopy and X-ray diffraction on a single crystal under hydrostatic conditions at room temperature. A soft mode is observed up to $P_c = 13.9(1)$ GPa. At this pressure, an isostructural phase transition between two monoclinic phases M_1 and M_1' hinders this instability. The features of this transformation (no apparent volume jump) indicate that the compression at ambient temperature passes close to a critical point. An analysis based on the Landau theory of phase transitions gives a complete description of the P-T phase diagram. The M_1' is characterized by spontaneous displacements of the oxygen sub-lattice without any strong modification of the VV dimers distances nor the twist angle of vanadium chains. The spontaneous displacements of oxygen and the spontaneous deformations of the (b_{M_1}, c_{M_1}) plane follow the same quadratic dependence with pressure and scales with spontaneous shifts of the Raman phonons located at 225, 260 and 310 cm⁻¹. Pressure-induced shifts of the Raman peaks allows for new assignment of several Raman modes. In particular, the $A_g(1)+B_g(1)$ modes at 145 cm⁻¹ are identified as the vanadium displacive phonons. A second transformation in the metallic phase X, which is found triclinic ($P\bar{1}$) is observed starting at 32 GPa, with a wide coexistence region (up to 42 GPa). Upon decompression, phase X transforms, between 20 GPa and 3 GPa, to another phase that is neither the M_1' nor M_1 phase. The structural transitions identified under pressure match with all the previously reported electronic modifications confirming that lattice and electronic degrees of freedom are closely coupled in this correlated material.

1. Introduction

VO₂ is a well-known prototypical electron-correlated material, showing a Metal-to-Insulator Transition (MIT) at ambient pressure and moderate temperature $T = 340$ K [1] accompanied with a structural phase transition. Despite VO₂ is already used in a variety of technological applications, such as infrared detection, thermochromics, transistors or microactuators (see the reviews [2,3,4]), the microscopic mechanism of the MIT is still an open fundamental question and a challenge for finding accurate functionals for theoretical DFT calculations [5,6]. Two mechanisms have been proposed and are still debated in many experimental and theoretical studies: the Peierls lattice distortion model and the Mott orbital electron model (or a mixture of both mechanisms) [7,8,9,10,11,12,13,14,15,16,17,18,19,20,21,22,23,24,25,26,27,28,29,30,31,32,33].

The associated structural transition from the metallic rutile structure ($P4_2/mnm$, n°136, $Z=2$ [34]) to the low-temperature insulating monoclinic ($P2_1/c$, n°14, $Z=4$ [35]), named M_1 , was explained by the phonon condensation at the R-point of the rutile Brillouin zone with vanadium displacements as the order-parameter (OP) [36, 37, 10, 11, 38, 39]. Thus, the metallic rutile structure is made of two vanadium chains with equal VV distances whereas the insulating monoclinic phase is characterized by two zigzagging chains with VV dimers. The thermodynamics of this displacive Peierls mechanism and the stability limits of the different phases were described in the framework of a Landau-type phenomenological model with a reduced two-dimensional component OP and free-energy expanded to six-degree, and eventually coupled with the strain [40, 41, 42, 43, 44, 45, 46, 32, 47]. This phenomenological description predicts the possibility of stabilizing other phases, such as a monoclinic $C2/m$ (n°12) phase, named M_2 , and an intermediate triclinic phase $P\bar{1}$ (n°2), named T (or M_3) [10, 38, 39]. These M_2 and T structures were observed in VO_2 doped with cation of lower oxidation states [48, 49, 50, 51, 52, 45] or under specific uniaxial stress [53, 34, 54, 55, 41, 42, 43, 56, 57, 58, 59, 60, 61, 46, 62]. The MIT was found to be remarkably affected by mechanical stresses [63, 64, 65] and a triple point between M_1 , M_2 and rutile phases was observed at 340 K at zero strain [40, 58].

Applying pressure is a relevant way to modify the stability between structural or electronic degrees of freedom. Thus, in M_1 phase of VO_2 , spectral discontinuities in both the mid-infrared optical conductivity and in the behavior of two Raman-active phonons located at 190 and 225 cm^{-1} [66, 67, 68, 69], observed at 10 GPa under quasi-hydrostatic pressure, were interpreted as vanadium dimers rearrangement [66]. Electrical discontinuity was also reported at 10-13 GPa [70, 71]. Synchrotron X-ray diffraction studies of pure VO_2 powders [72, 71, 69, 73] or nanoparticles [74] have shown that the M_1 phase transforms, above 11-13 GPa, to an isostructural phase (same space group $P2_1/c$ n°14, $Z=4$), named M_1' . Since there is no apparent change in the crystal symmetry, the transition pressure is defined by a discontinuity in the compression behavior of the (b_{M1}, c_{M1}) monoclinic plane [72, 71, 69, 74]. Contrary to early studies, Bai et al. proposed that the discontinuities measured at the M_1 - M_1' transition in the pressure dependence of the Raman modes located at 190, 225 and 320 cm^{-1} are not associated to any V-chains rearrangement [71]. The persistence of the VV dimerization up to 22 GPa and a VV pair twist angle remaining close to 3° was then confirmed by atomic pair distribution function analysis [75]. Density functional theory calculations suggested that the M_1 - M_1' transition is induced by an unstable Γ -point phonon that is related to the rotation of the oxygen octahedra along the monoclinic a_{M1} axis (or the parent rutile c_R axis) [76]. In their calculations, the pressure-induced reduction of the band gap and metallization is accounted by clockwise rotations (phase M_1'') that progressively reduce the dimerization and zigzags of the vanadium chains [76].

At higher pressure, a second phase transition to a metallic phase X was detected (between 28-50 GPa). The slope change [69] or splitting [71] of the Raman mode at 225 cm^{-1} , observed above 27.8 GPa, was assigned to phase X. Afterwards, Balédent et al. observed this splitting at 19 GPa and proposed a new insulating M_3 phase, different from the metallic phase X [73]. Different structures have been proposed for phase X such as a monoclinic baddeleyite-type ($P2_1/c$, n°14) with $Z=8$ [71, 69] or with $Z=4$, named Mx [74, 77] in which the vanadium coordination number increases from six to seven. Xie et al. proposed that a different seven-coordinated orthorhombic structure ($Pmn2_1$, n°31, $Z=2$) coexists with the low-pressure M_1 between 29 and 79 GPa [78]. A different monoclinic space group (Pn , n°7) was inferred using spin-polarized *ab initio* structure search [73]. Under decreasing pressure, another monoclinic baddeleyite-type polymorph, named Mx' , was reported following a high-pressure treatment of the M_1 phase up to 63 GPa [74, 77]. Additional pressure measurements, at 383 K [71], or on W-doped VO_2 [79], have shown that rutile phase transforms at 13.3 GPa to an orthorhombic $CaCl_2$ -type structure ($Pnmm$, n°58, $Z=4$) and coexists with metallic phase X between 32 and 64 GPa. The pressure-temperature phase

diagram of VO₂ was built using Raman, optical reflectance and electrical transport characterizations [80].

Therefore, although many experimental and theoretical calculations were published concluding on the presence of several different M₁' , M₁'', M₃, phase X, Mx and Mx' structures under increasing pressure, no agreement has yet been reached on the phase sequence under high pressure and on the associated mechanisms. One of the reasons lies in the experimental limitation due to the form of the sample (powder, nanobeams) and quasi-hydrostatic conditions that can play a significant role. The aim of this study is to present new results obtained by Raman and X-ray diffraction analysis on a high-quality VO₂ single crystal compressed under hydrostatic conditions using Helium as the pressure-transmitting medium. In a first section, X-ray diffraction data obtained during compression will be displayed. These make it possible to clarify the phase transition sequence and the microscopic mechanism involved. Then, Raman spectroscopy measurements will be presented with new insights in terms of assignment and pressure-induced behaviour. A phenomenological analysis will be proposed to describe the experimental P-T phase diagram of VO₂. In the last section, the obtained results are combined to correlate the behaviours of the Raman modes with the strains and microscopic characteristics of the compound. This will be of interest to characterize phases in thin films of (doped) VO₂ and the nature and amplitude of the strains.

2. Experimental

High-quality crystals with natural faces of stoichiometric VO₂ crystals were produced by chemical vapour transport, using TeCl₄ transport agent and following the procedure described in Ref. [81].

High-pressure experiments were performed using a membrane driven diamond anvil cell (DAC) with 250/300 μm bevelled diamond culets. A pressure chamber of 160 μm in diameter and 40 μm in thickness was drilled in a stainless-steel gasket. Helium, loaded at 1.4 kbar, was used as the pressure transmitting medium to ensure high hydrostatic pressure conditions up to 42 GPa, the highest pressure reached in this study. During the Raman experiment, the pressure was measured using the R₁-line emission of a ruby ball placed close to the sample using Holzapfel equation of state [82]. The ruby signal is measured before and after each measurement in order to control the pressure drift during long acquisitions. The recorded pressure is set at the average of these two pressure values and the uncertainty is set as the half of the difference between these two values. The homogeneity of the pressure in the DAC was followed from both the width and the splitting between the R₁ and R₂ ruby lines [83, 84]. During the X-ray diffraction experiment, the pressure was measured using the equation of state of pure copper powder [85] placed close to the crystal. The copper X-ray diffraction images were integrated with the Dioptas software [86].

Three experiments on two different single crystals were done. During the first one, we recorded only Raman on a crystal of 40x30 μm in size and 10 μm in thickness up to 42 GPa and back to room pressure. We have reproduced this Raman experiment on a smaller crystal of 15x18 μm and 10 μm thickness up to 25 GPa and back to room pressure. During this second experiment, we have chosen not to exceed 25 GPa in order to avoid forming the high-pressure metallic phase. A third experiment up to 35 GPa, using X-ray diffraction was done with the second crystal that had already experienced pressure during the second Raman experiment.

The ruby and Raman measurements were made at room temperature using a 514.4 nm laser (Cobolt Fandango) and a 750 mm spectrometer (SP2750, Acton Research) with a 2400 grooves/mm grating (blazed at 500 nm), equipped with a cooled CCD camera (PyLoN, Princeton), and a 50 μm entrance slit size that provides a resolution of 0.70 cm⁻¹ (0.019 nm). A set of Bragg filters (BNF-Optigrate) were used

in order to reject the excitation line. The spectra were recorded in backscattering geometry with a 50X objective (Nikon) to focus the incident laser beam and collect the scattered light from inside the DAC through the diamond anvil. The spectrometer was calibrated in wavenumber using the lines of a Ne-Ar lamp. The incident laser power was fixed at 0.5 mW (measured before the DAC) in order to avoid any laser heating of the sample that could induce the M_1 -Rutile transition at 340 K. The Raman spectra covering a 25–900 cm^{-1} spectral range were recorded using two monochromator positions with a maximum of 300 s acquisition time averaged over two to four acquisitions. In the 25-150 cm^{-1} range, we have subtracted the contribution of N_2/O_2 rotations lines. Spectral parameters (position and full-width at half maximum FWHM) were obtained from the decomposition of each spectrum with several Lorentzian peaks using Fityk software (version 1.3.1) [87].

Single crystal X-ray diffraction (XRD) experiment was done at ID15B beamline (ESRF Grenoble) with a monochromatic wavelength $\lambda=0.41020 \text{ \AA}$ and a $2 \times 4 \mu\text{m}$ focused beam. Diffraction images were collected during the continuous rotation of the DAC around the vertical ω axis in a range $\pm 32^\circ$, with an angular step of $\Delta\omega=0.5^\circ$ and an exposure time of 0.5 s/frame. The CrysAlis^{Pro} software package [88] was used for the analysis of the single-crystal XRD data (indexing, data integration, frame scaling, and absorption correction). A single crystal of Vanadinite [$\text{Pb}_5(\text{VO}_4)_3\text{Cl}$, $Pbca$ space group, $a = 8.8117(2) \text{ \AA}$, $b = 5.18320(10) \text{ \AA}$, and $c = 18.2391(3) \text{ \AA}$] was used to calibrate the instrumental model in the CrysAlis^{Pro} software, i.e., the sample-to-detector distance, detector's origin, offsets of the goniometer angles, and rotation of both the X-ray beam and detector around the instrument axis. Using the Jana2006 software package, the structure was solved with the ShelXT structure solution program [89]. Crystal structure visualization was made with the VESTA software [90]. The equation of state was obtained by fitting the pressure–volume data using a third order Birch-Murnaghan (BM EoS). Le Bail profile analyses of the pattern measured at 35 GPa have been carried out using the FULLPROF software [91]. Cell parameters and overall thermal factor are refined. The background was first removed with a spline interpolation and then refined as a linear function. The peak shape was described with pseudo-Voigt function. The profile parameters u, v, w and the mixing parameter of the pseudo-Voigt function were kept fixed for the final refinement.

3. Results

3.1. Single crystal X-ray diffraction under high-pressure

The single crystal diffraction measured in the restricted geometry of the DAC allows to index 180 peaks ($\sim 30\%$ of the total reciprocal lattice) in a monoclinic reduced niggly-cell with $a_{M_1} = 5.3548(6) \text{ \AA}$, $b_{M_1} = 4.5253(2) \text{ \AA}$, $c_{M_1} = 5.3817(3) \text{ \AA}$, $\beta_{M_1} = 115.224(9)^\circ$ and volume $V_{M_1} = 117.974(15) \text{ \AA}^3$ with space-group $P2_1/c$ ($n^\circ 14$, $Z=4$, cell choice 1). Notice that this reduced cell is identical to the $P2_1/n$ ($n^\circ 14$, $Z=4$, cell choice 2) monoclinic cell with $a_{M_1} = 5.7510(8) \text{ \AA}$, $b_{M_1} = 4.5253(17) \text{ \AA}$, $c_{M_1} = 5.3548(6) \text{ \AA}$, $\beta_{M_1} = 122.16(2)^\circ$ in agreement with the lattice parameters reported in the ICSD [35] for phase M_1 . The reciprocal maps attest to the absence of multi domains in the crystal measured under pressure (see Figure S1 in the supplementary information). Unfortunately, the orientation of the crystal in the DAC was not favourable to access to the $[0k0]$ direction in the $(hk0)$ plane and to confirm the presence of the 2_1 -screw axis along the b axis. However, the specific extinctions $(h0l)$ with $h+l=2n$ and $(h00)$ with $h=2n$ due to the presence of a mirror n perpendicular to the b axis are observed. The crystallographic extinctions are not modified up to 34 GPa (Figure S2) which discard any structural transition to $P\bar{1}$ ($n^\circ 2$), $P2_1$ ($n^\circ 4$), or Pc ($n^\circ 7$) subgroups of the $P2_1/c$ space group. The diffraction intensities are refined in the M_1 phase (see the refinement parameters at 0.3 GPa in Table S1). The crystallographic parameters (unit cell parameters, volume and atomic positions) up to 34 GPa are given in Table S2.

Figures 1(a-d) display the monoclinic unit cell parameters evolution with increasing pressure. As observed previously [72, 71, 69, 74], the a_{M1} lattice parameter decreases without any detectable discontinuity between 0 and 34 GPa whereas, above 13-14 GPa, a discontinuity is observed in the (b_{M1} , c_{M1}) monoclinic plane, i.e., the b_{M1} softens while the c_{M1} hardens simultaneously. A discontinuity is also observed in the pressure behavior of the beta angle at 14 GPa (see Fig 1c). The non-linear pressure dependence of cell parameters are reproduced by a third order Birch-Murnaghan-like equation of state (BM EoS) with $a_{M1}^{\circ} = 5.7506(7) \text{ \AA}$, $K^{\circ} = 545(5) \text{ GPa}$ and $K' = 4.9(3)$ between 0 and 34 GPa and by three second order BM-like EoS with $b_{M1}^{\circ} = 4.5259(7) \text{ \AA}$, $K^{\circ} = 630(9) \text{ GPa}$, $c_{M1}^{\circ} = 5.3521(12) \text{ \AA}$, $K^{\circ} = 820(23) \text{ GPa}$ and $\beta^{\circ} = 122.16(1)^{\circ}$, $K^{\circ} = 12672(682) \text{ GPa}$ between 0 and 13 GPa. Below 14 GPa, the monoclinic a_{M1} cell parameter is more compressible than the b_{M1} and c_{M1} parameters and the beta angle is remarkably stiff. Using the EoS of the low pressure M_1 and extrapolating them above 14 GPa, the elastic spontaneous deformations e_{11} , e_{22} , e_{33} , e_{12} , e_{13} , e_{23} and the $e_{\text{total}} = \sqrt{\sum e_{ij}^2}$ are calculated in the high-pressure monoclinic phase. The e_{11} , e_{12} , e_{13} , e_{23} stay at values close to zero whereas the e_{22} , e_{33} and e_{total} increase as the square root of (P-P_c) as shown in Figure 2. Maximum values of $e_{22} = -1.5\%$, $e_{33} = +2.5\%$ and $e_{\text{total}} = +2.9\%$ are reached at 34 GPa.

The pressure dependence of the volume shown in Figure 3(a), did not show any obvious discontinuity in the whole pressure range. The volume variation was first fitted with one unique third order BM EoS with $V_0 = 117.97(4) \text{ \AA}^3$, $K^{\circ} = 214(2) \text{ GPa}$ and $K' = 2.5(1)$ between 0 and 34 GPa. However, the value of K' less than 4 and the discontinuity at 13-14 GPa in the F-f plot reveal the structural transition (see insert in figure 3(a) using $V_0 = 117.97 \text{ \AA}^3$). Thus, the EoS of M_1 phase are $V_0 = 118.00(4) \text{ \AA}^3$, $K^{\circ} = 194(7) \text{ GPa}$ and $K' = 7(1)$ between 0 and 14 GPa and $V_0 = 119.6(6) \text{ \AA}^3$, $K^{\circ} = 162(17) \text{ GPa}$ and $K' = 4.6(8)$ between 14 to 34 GPa. The EoS of M_1 and M_1' phases agree with Ref. [71]. The K° values are 15% lower than those measured on nanoparticles [74]. The distance between the two vanadium atoms of VV dimers along the monoclinic chain shows a regular decrease with pressure from 2.62 \AA to 2.47 \AA at 34 GPa (see Figure 3(b)) and is fitted by a third order BM-like EoS with $d_{\text{VV}}^{\circ} = 2.6199(8) \text{ \AA}$, $K^{\circ} = 564(14) \text{ GPa}$ and $K' = 2.3(8)$. A maximum contraction of 5.7% is measured at 34 GPa. As shown in Figure 3(c) the VO_6 polyhedra reduce their volume without any apparent discontinuity at 14 GPa and can be reproduced by a third order BM EoS with $V^{\circ}_{\text{octa}} = 9.542(6) \text{ \AA}^3$, $K^{\circ} = 173(5) \text{ GPa}$ and $K' = 12.2(7)$. A maximum contraction of 10% is measured at 34 GPa. The individual VO distances inside an octahedron, reported in Figure S3, show a regular decrease with the tendency for the VO_6 polyhedron to become more symmetric.

The relative variation of the atomic fractional parameters with pressure obtained from refining the single crystal diffraction intensities indexed in space-group $P2_1/n$ ($n^{\circ}14$, $Z=4$, cell choice 2) are reported in Figure 4. Vanadium and oxygen atoms are in general position (site 4e). The vanadium coordinate along b_{M1} increases continuously by 0.4(1)% at 34 GPa. They decrease by 0.3(1)% at 14 GPa in the (a_{M1} , c_{M1}) plane and remain constant above. The two oxygen fractional positions almost do not change in the pressure range 0-14 GPa, but they display a clear deviation above 14 GPa that is one order of magnitude larger than that of the vanadium displacements. In figure 4(b), we report the spontaneous displacements of both oxygens atoms measured along the three crystallographic directions after subtracting the displacements extrapolated from the behavior below 14 GPa. Notice that both oxygen atoms display opposite spontaneous displacements of the exact same amplitude along a_{M1} (former c_R axis in the rutile phase) and c_{M1} directions while they move in the same direction along b_{M1} (former a_R axis in the rutile phase). The oxygen spontaneous displacements follow a square root dependence with P-P_c with fixed P_c=13.9 GPa as plotted with plain lines in figure 4(b).

At 35 GPa, the previous well resolved single crystal diffraction pattern disappeared suddenly. The crystal is damaged which indicates a first order transition. Some crystallographic axes are still observed;

however, Bragg peaks are spread in the azimuthal direction (see insert in Figure 5). Different structural models (including baddeleyite-type phase X from ref [71], Mx from ref. [74,77], or orthorhombic phase from ref [78]) were tested but none of them can reproduce the X-ray diffraction pattern. The pattern was indexed with a triclinic ($P\bar{1}$) cell with $a=9.075(3)$ Å, $b=4.412(2)$ Å, $c=4.996(3)$ Å, $\alpha=87.84(4)^\circ$, $\beta=94.52(4)^\circ$, $\gamma=92.67(4)^\circ$ and $V=199.05(19)$ Å³ with Bragg R factor of 0.4% as reported in Figure 5. The unit cell contains height VO₂ formula unit. A volume jump of $\Delta V/V=-3.3(1)$ % is measured at the transition. The high-pressure phase X is different from the structural model reported for the triclinic phase in VO₂ doped with cation of lower oxidation states or under uniaxial stress. If it was the case, we would expect a second order continuous transition that is not observed. Attempts were made to refine the structure starting from a baddeleyite-type model but the statistics in azimuthal direction was not good and the intensity was too low to obtain a reliable refinement.

3.2. Single crystal Raman spectra under high-pressure

The Raman spectrum measured on a VO₂ single crystal is identical to previously published spectra for the M₁ phase [92,93,94,95,96,97]. Eighteen Raman active modes (9A_g+9B_g) are expected and almost all of them were identified at 83 K on a naturally oriented single crystal [93,94] (Table 1). Figure 6 displays a zoom on the low wavenumber part of the Raman spectra (70-340 cm⁻¹) to highlight the softening/hardening of the low-laying 145 cm⁻¹ weak mode observed under pressure. The Stokes and anti-Stokes spectra measured at 21 GPa (see figure S5) confirm that this mode is a phonon and not a fluorescent artefact. The entire Raman spectra measured up to 25 GPa, are reported in figure S4. In this work the Raman modes are labelled as A_g(1) to A_g(9), and B_g(1) to B_g(9) in Figure 6 and in Figure S4.

Figure 7 presents the pressure dependence of spectral parameters obtained from the decomposition of Raman spectra with Lorentzian functions. In the past studies, the symmetry assignment of lowest wavenumber mode at 145 cm⁻¹ was not conclusive (A_g, B_g or the superposition of both symmetries was proposed) [96,97] (Table 1 gather the different assignment proposed in the literature). Here, thanks to the different pressure dependences, we confirm that, at ambient conditions, one soft mode and one hard mode with different symmetries are superimposed at 145 cm⁻¹. At pressure above P_c= 13.9(1) GPa, the soft mode changes its behavior and starts hardening, which marks the isostructural M₁-M₁' transition. This transition is reversible with no pressure hysteresis. Extrapolating the $v_{SM}^2(P)$ to $v_{SM}=0$ limit gives P_c^{*}= 26.9(4) GPa, for the potential stability limit of the M₁ phase. The ratio between the slopes dv^2/dP below and above P_c is 2.4(1) close to 2, characteristic of a continuous phase transition. With increasing pressure, the hardening mode successively cross the A_g(1) mode at 25 GPa, and the 190 cm⁻¹ A_g(2) mode at 29.5 GPa, and shows a deviation from the linear dependence at pressure higher than 32 GPa before disappearing at 41 GPa (Figure 7(a)). The spectra recorded between 20 and 29 GPa showing the successive crossing between low wavenumber modes are reported in figure S6(a). The pressure evolution of the half width at half maximum (HWHM) of both B_g(1) and A_g(1) modes obtained from the decomposition of the Raman spectra using Fityk software are reported in figure S6(b). The B_g(1) HWHM is narrower (2 cm⁻¹) than the A_g(1) (6 cm⁻¹). Under pressure, the HWHM of B_g(1) remains constant as A_g(1) decreases sharply. Above 20 GPa, depending on experience and therefore local conditions, HWHM may fluctuate, but as far as positions are concerned, everything is reproducible. The integrated intensity (area) progressively increases with pressure above P_c (Figure 7(b)). Contrary to previous studies [66,67,68,71,73], the A_g(2) mode at 190 cm⁻¹ does not show any abrupt increase is the rate dv/dP at P_c. We rather measured a small decrease of the slope from $dv/dP= 0.36(1)$ cm⁻¹/GPa to 0.22(1) cm⁻¹/GPa at the transition. The discontinuity reported at 10 GPa in previous studies might be a consequence of the use of non-hydrostatic pressure transmitting media, i.e. NaCl, KCl [66,67], or ethanol-methanol [68,69,80] that are known to be strongly anisotropic at this pressure. The half width at

half maximum, HWHM, (Figure 7(d)) shows a regular decrease with pressure up to 29 GPa, followed by a tendency to increase that is always observed at such high pressure because of the progressive loss of hydrostaticity of the helium transmitting medium. The same tendency is measured on the ruby pressure marker (see Figure 7(d)). The integrated intensity (area) of the $A_g(2)$ peak (Figure 7(c)) is almost constant up to 32 GPa and suddenly drops at higher pressure before disappearing at 41 GPa. The pressure dependences dv/dP and the Grüneisen parameters of the Raman modes are reported in Table 2 and their positions are given at 0 GPa for the M_1 phase and at 13.9 GPa for the M_1' high-pressure phase.

A second original observation in Raman spectra of the M_1 phase under pressure is the splitting of the mode at 225 cm^{-1} in two components at pressure as low as 3 GPa within the resolution limit of our spectrometer (see Figure 7(a) and figure S7). This mode was in the past associated to a single A_g symmetry but experimental [97] and theoretical studies [98, 99] have proposed that two modes of A_g and B_g symmetries could be superimposed at room condition. Here again, pressure allows for distinguishing both modes due to their different pressure-dependences. Both modes show a sharp slope changes in $\nu(P)$ at $P_c = 13.9(1)$ GPa (see Table 2).

The variations of the spectral features at the transition allows for correlating the Raman modes with the different components of the strain. The spontaneous shift $\nu(M_1') - \nu(M_1)$ is calculated after subtracting the wavenumber $\nu(M_1)$ extrapolated above P_c from the behavior measured below 14 GPa. The $A_g(3)$ scales linearly with the absolute value $|e_{22}|$ of the spontaneous strain along b_{M1} (Figure 8(a)) or with $(e_{33}-e_{22})$ that reflects the deformation of the (b_{M1}, c_{M1}) plane. The $B_g(3)$ scales linearly with the square of the spontaneous strain along c_{M1} (e_{33}^2) (see Figure 8(b)). With further increasing pressure, at 29 GPa, another discontinuity is observed in the splitting (see figure S7). In previous studies, the splitting was observed, only above 27-28 GPa [71, 69] or above 19 GPa [73] but was associated to phase X or to a new insulating M_3 phase, different from phase X.

A third original observation in the M_1 phase, concerns the Raman modes $B_g(2)$ at 260 cm^{-1} , and $A_g(4)$ at 310 cm^{-1} . They exhibit an unusual small pressure-dependence of their positions (see Figures 9(a) and 9(b)). The slopes are $dv/dP = 0.03(1)\text{ cm}^{-1}/\text{GPa}$ and $dv/dP = 0.13(1)\text{ cm}^{-1}/\text{GPa}$, respectively (see Table 2). However, they show an abrupt change in their dv/dP at P_c . To the best of our knowledge, the $B_g(2)$ slope discontinuity was never reported. Some authors have seen that this mode disappear between 14-15 GPa [71, 69] or at 22 GPa [74]. From our observations, the intensity starts decreasing at 14 GPa but the mode is still observed up to 30 GPa. The slope changes of the $A_g(4)$ mode was reported at the M_1 - M_1' transition above 13 GPa [71, 74]. The HWHM (not shown) exhibits a regular decrease with increasing pressure similar to that measured on the $A_g(2)$ mode (Figure 7(b)). The spontaneous shift $\nu(M_1') - \nu(M_1)$ for the $A_g(4)$ mode scales linearly with e_{33}^2 (Figure 9(c)).

The Raman modes at higher wavenumbers exhibit classical increase of their positions with increasing pressure (see figure S8). The slopes dv/dP are larger than those measured for the low-wavenumber modes. A small decrease of the slopes dv/dP is observed at P_c (see Table 2). Notice that the slope of the $B_g(4)$ mode, at 340 cm^{-1} and $B_g(8)$ mode, at 665 cm^{-1} are almost not affected by the transition at P_c .

At 32 GPa, the collapse of the Raman intensity and the sudden increase of the background are the signature of the formation of the metallic phase X. With further increasing pressure up to 41 GPa, the Raman peaks disappear and some new peaks appear progressively. The Raman signature of the pure phase X recorded during decompression is reported in Figure 10 (in red at 28.7 GPa) and shows nine weak peaks at 185, 325, 440, 466, 505, 662, 707, 763 and 845 cm^{-1} (see Fig. 10 and Fig. S8). Upon decompression, the Raman spectra show a transformation, between 22 and 18.5 GPa, to a spectrum of reasonable intensity that is not compatible with neither the M_1' nor M_1 structures but can be

explained by a coexistence between phase X and a new structure. The coexistence persists down to 9.3 GPa but, between 5 and 3 GPa, phase X completely disappeared and the remaining spectrum resembles that of the triclinic T phase (or M_3) measured on 0.7% Cr-doped VO_2 by Marini et al. [67]. The same signature was reported on VO_2 nanoparticles below 23.9 GPa and down to 2.1 GPa by Li et al. [74], and was interpreted as a back transformation from the baddeleyite-type M_x phase into a new baddeleyite-type M_x' phase with a local structure similar to the M_1 structure.

4. Discussion

4.1. First transition from M_1 to M_1' at 14 GPa

Depending on the pressure transmitting medium, the M_1 - M_1' transition has been reported at pressure varying between 10 and 15 GPa [66,67,68,72,71,74,80]. In our hydrostatic conditions, VO_2 single crystal exhibit a first isostructural transition, M_1 to M_1' , at $P_c = 13.9(1)$ GPa as observed by Raman and x-ray diffraction measurements. The transition is quasi-continuous, second order-like with no measurable volume jump. The transition is displacive with oxygen displacements compatible with the R-point condensation (in the parent rutile) without strong modification of the VV dimers nor of the twist angle of vanadium chains (Fig. 4). The oxygen sub-lattice spontaneous displacements and the spontaneous deformation of the (b_{M_1}, c_{M_1}) plane follow the same quadratic dependence with pressure (Fig. 2 and 4). The monoclinic a_{M_1} lattice parameter is not affected by the transition (Fig. 1).

We can combine these new high-quality experimental data with reliable information published so far, and suggest therefore a coherent picture of phase transitions in VO_2 compressed and heated/cooled. The rutile to monoclinic transition is an *improper ferroelastic transition of displacive type* and is induced by the four-component order-parameter spanning R_1^- irreducible representation at the R-point of the tetragonal Brillouin zone [36, 37, 10, 11, 38, 39, 47]. Mechanical (vibrational) representation of the rutile-type structure at the R-point of the Brillouin zone reads:

$$T_M = (3R_1^-)_V + (3R_1^- + 3R_1^+)_O \quad (1)$$

Thus, the symmetry-breaking atomistic mechanism of the structural R- M_1 transformation contains simultaneous vanadium and oxygen atoms displacements, both transforming as R_1^- and, therefore, coupled bilinearly in the free-energy. In other words, the symmetry lowering and distortion of the tetragonal structure are controlled by coupled vanadium and oxygen displacements. In the high-temperature rutile phase, the four components of the R_1^- OP are zero: $\eta_1 = \eta_2 = \eta_3 = \eta_4 = 0$, and the vanadium chains are regularly aligned with fixed VV bonds distances of 2.86 Å. At the rutile to M_1 transition, one component of the R_1^- OP takes non-zero value ($\eta_1 \neq 0, \eta_2 = \eta_3 = \eta_4 = 0$). The R-point imposes that two antiferroelectric vanadium displacements occurs when $\eta_1 \neq 0$: one along the a_{M_1} axis ($a_{M_1} = 2c_R$) forming VV dimers on one chain and one off-axis in the plane perpendicular to a_{M_1} axis forming twisted vanadium on the nearest neighbor vanadium chain [10, 47]. Thus if $\eta_1 \neq 0$ two twisted vanadium chains with VV dimers are formed in the M_1 phase.

Under pressure, the second component η_2 of the R_1^- OP, which reduces its symmetry to $B_g(1)$ after the Brillouin zone folding, drives the structure transformation to the M_2 phase with: $\eta_1 = \eta_2 \neq 0$ ($\eta_3 = \eta_4 = 0$). One set of vanadium chains pair (VV dimers) is not twisted while the other set stays twisted but loses the VV dimers. The M_2 phase is expected at 27 GPa, as estimated from extrapolating the linear part of the soft mode wavenumber $\nu_{SM}^2(P)$ measured experimentally to the $\nu_{SM}=0$ limit. However, the M_2 phase is not observed because the isostructural M_1 - M_1' transition occurs at $P_c = 13.9(1)$ GPa suppressing this instability and conserving the M_1 -type phase thermodynamically more stable. The observed phonon softening does not drive the M_1 - M_1' transition (but drives the M_1 - M_2). The isostructural transition somehow prevents the M_1 - M_2 transition from taking place under

hydrostatic pressure as detailed in the Landau-based analysis developed in the next section. The oxygen displacements and the monoclinic (b_{M1} , c_{M1}) plane distortion remind those found in the rutile to CaCl_2 transition observed in VO_2 at higher temperature [71, 79, 80] and in many other AO_2 oxides. However, the oxygen polyhedron is not only rotating along to the a_{M1} axis (former c_R axis in the rutile phase). Let us show, in the framework of phenomenological theory, that the reason for the isostructural transition lays in the highly anharmonic dependence of the free-energy on the non-totally-symmetric OP.

4.2. Understanding the VO_2 phase diagram from phenomenological theory

Our experimental findings allow us to derive a complete picture of phase transitions in VO_2 observed under different pressure and temperature conditions ($P < 35$ GPa). This requires to consider two-component effective order-parameter. The image-group, reduced form of the relevant four-dimensional representation R_1^- to a two-dimensional effective order-parameter group, possesses the point-symmetry $4mm$. Phenomenological models for the two-dimensional tetragonal image-group were analysed in detail by Y. Gufan and co-workers and cited in [100].

The basic invariants forming the integrity basis for the image-group $4mm$ are:

$$I_1 = \eta_1^2 + \eta_2^2, \text{ and } I_2 = \eta_1^2 \cdot \eta_2^2. \quad (2)$$

Accordingly, the most compact structurally stable order-parameter ten-degree expansion, which is necessary to account for two consecutive first-order phase transitions R - M_1 and M_1 - M_1' (see Appendix 1), is expressed as:

$$F(\eta_1, \eta_2, P, T) = a_1(P, T)I_1 + a_2(P, T)I_1^2 + b_1I_2 + c_{12}I_1I_2 + a_4I_1^4 + b_2I_2^2 + a_5I_1^5. \quad (3)$$

The free-energy (3) has four minima corresponding to the four phases known for VO_2 :

- I: $\eta_1 = \eta_2 = 0 \sim R$;
- II: $\eta_1 \neq 0, \eta_2 = 0 \sim M_1$;
- III: $\eta_1 = \eta_2 \neq 0 \sim M_2$;
- IV: $\eta_1 \neq \eta_2 \neq 0 \sim T$.

Figure 11 shows a section of the theoretical phase diagram, corresponding the potential (3), which is topologically adequate to understand the VO_2 pressure-temperature phases diagram experimentally mapped in hydrostatic conditions. In addition, this free-energy expansion includes the existence of a critical end-point K (gas-liquid type) on the M_1 - M_1' transition line at which the first-order transition transforms to a cross-over continuous regime (see annex 1). The fact that no apparent volume could be experimentally measured indicates that the isostructural M_1 - M_1' transition is quasi-continuous and reveals that the pressure path passes in close vicinity of this critical point K (Figure 11). Varying pressure at higher temperature should allow to measure an increasing volume jump at the M_1 - M_1' transition as one moves away from the critical point. The topology of the phenomenological phase diagram also predicts that the triclinic T structure can be observed at even higher hydrostatic pressures. On the contrary, M_2 and rutile R phases might hardly be formed under hydrostatic pressure at ambient temperature. The phase diagram explains also that Cr-doped VO_2 , which adopt triclinic (for 0.7% Cr) or M_2 (for 2.5% Cr) phases, are reported to first transform to M_1 phase at 2.7 GPa and 3.7 GPa, respectively, and then, to the same M_1' phase as pure VO_2 at 12 GPa [67, 72].

It is worth stressing that the general form of Eq. (3) and the diagram shown in Figure 11 are generic ones since they also account for stress/strain effects. Indeed, we can distinguish two types of strain components: (i) through improper spontaneous strains induced by the primary order-parameter R_1^-

(e_{11} , e_{22} , e_{33} , e_{12} , and e_{13}), and (ii) through external deviatoric stress (e_{23}) developing under quasi-hydrostatic compression conditions, or surface effects in thin films, for instance [41, 42, 43]. Although the coupling terms in the free-energy have different forms, $\eta_i^2 \cdot e_{jk}$ and $\eta_i^2 \cdot e_{lm}^2$, they should be integrated with the unique quadratic invariant I_1 in the free-energy (3). This will lead to renormalizing the corresponding coefficient ($a_1+c_{ij}+c_{ii}$) $\rightarrow \tilde{a}_1$ but without modifying the general form of Eq. (3). The topology of the phase diagram of Fig.11 remain unchanged, however the transition line can be shifted and then the M_2 phase could be observed under non-hydrostatic stress. Topology means the correct description of the phases in contact, and prediction of the order for the phase transition that can occur between them.

The changes in the midinfrared transmittance/reflectance [66, 67, 68, 69] and in the resistivity observed previously under pressure [71, 70, 80] are concomitant with the M_1 - M_1' isostructural transition. This strongly suggests that electronic properties and structural modifications (with oxygen displacements) are linked and that the Peierls mechanism is valid. We can assume that this isostructural transition can also be induced by uniaxial/bi-axial stresses in thin films, or in non-stoichiometric VO_2 for which internal stresses can be generated. Thus, experimental studies that have questioned the Peierls mechanism because of the observation of a monoclinic-like metallic VO_2 where electronic and structural transitions seem decoupled [101, 102, 103, 104] did not consider the possibility of having formed the isostructural M_1' phase.

4.3. Raman signature of M_1 , M_2 or T phases as a tool for thin film engineering

The technological interest on VO_2 has led to the study of various thin films or nanobeams using Raman spectrometry as a valuable tool to differentiate between rutile, M_1 , M_2 or T phases [105, 55, 45, 57, 106, 107, 108, 45, 97, 30, 109]. The metallic rutile has a weak signal composed of broad modes at 300 and 550 cm^{-1} (for $A_{1g}+B_{1g}+E_g$) [110] that are difficult to measure. The Raman signature of M_1 is quite well documented but not all the $9A_g$ and $9B_g$ modes were observed and the symmetry assignments are still being debated (see Table 1). The present study, thanks to pressure-induced variations of the peak positions allows for clarifying the assignment (see section 3.2). Moreover, very few is known on the atomic displacements (eigenvectors) involved in each mode. Since the Raman study under oxygen isotopic substitution [67], it is often said that the two intense low wavenumber modes at 190 and 225 cm^{-1} involve predominantly vanadium displacements. This was supported by the phonon density of state obtained with *ab initio* calculations [111, 98, 112, 99, 6, 113]. There is a widespread belief that these modes are associated with the stretching and twisting features of the dimerized chains and contribute to the M_1 -rutile transition [17, 67, 111, 98, 69, 99]. However, these modes do not obviously soften at the MIT [92, 13, 94]. The Raman signature of the T phase is similar to that of M_1 but the $A_g(1)$ mode is downshifted to 126 cm^{-1} , the $A_g(2)$ is upshifted to 200 cm^{-1} , and a small splitting of the $A_g(3)+B_g(3)$ is observed [67, 45, 106, 114, 115, 116, 117]. In the M_2 phase, the $A_g(1)$ mode downshifts even more to 50 cm^{-1} , the $A_g(2)$ stays at 200 cm^{-1} , and two components are clearly observed for the $A_g(3)+B_g(3)$ [67, 105, 55, 45, 57, 106, 108, 116]. We do not endorse the fact that the $A_g(1)$ mode could be a breathing mode of spin-Peierls dimerized 1-D spin $\frac{1}{2}$ Heisenberg chain [116] but rather found that the two modes $A_g(1)+B_g(1)$ at 145 cm^{-1} are the vanadium displacive modes expected from the condensation of the Rutile R_1^- OP. The progressive softening of the $A_g(1)$ mode through M_1 to T and M_2 structural transformation, where one half of the the Peierls pairing and twisting are partially removed or with increasing pressure, where only one mode softens until the transition to M_1' hinders this instability, supports our finding.

The splitting of the $A_g(3)+B_g(3)$ mode, at 225 cm^{-1} , in both M_1 and M_1' phases, highlighted in Figures 7(a) and Figure S7, was often misunderstood in the past. Several DFT calculations concluded that the zigzag V motions that untwist the VV pairs are located between 6.0 THz (197 cm^{-1}) [98], 6.38 THz (213 cm^{-1})

[¹¹¹] or 26.5 THz (217 cm⁻¹) [¹¹⁸], close to the positions of the A_g(3)+B_g(3) modes. We do not observe any softening with pressure and doubt that these modes are linked to the pairing or tilting motions of VV dimers. We found that the splitting is observed in the M₁ phase at 2-3 GPa (Figure 7(a)). Indeed, from the linear pressure evolution of each mode, we found that the two modes intersect at 1.9 GPa confirming they have different symmetries. The angular dependence of the Raman intensity in different polarized conditions measured outside the DAC as shown in Figure S9, also show the superimposition of two different symmetries already in the M₁ monoclinic phase at ambient conditions in agreement with Shibuya et al. [⁹⁷]. The splitting is equal to 0.8 cm⁻¹ in the M₁ at room condition which explains why it was hardly detectable in past studies. At the M₁-M₁' iso-structural transition, both modes display an abrupt change of their dv/dP (see Figures 7(a) and S7 or in Table 2). We found that the A_g(3) scales linearly with the spontaneous strain along *b*_{M1} whereas the B_g(3) scales linearly with the spontaneous strain along *c*_{M1} (see Figure 8(a-b)). Thus, the A_g(3)+B_g(3) splitting is a good marker of the nature of the strain experienced by VO₂. The unusual pressure behaviour observed at 24-25 GPa (see Figure 7(a) and S7) is a consequence of the saturation of the spontaneous deformation along *b*_{M1} axis while the one along the *c*_{M1} increases without there being a phase transition. Quantification of the monoclinic deformation can also be done using either the A_g(4) mode at 310 cm⁻¹ or the B_g(2) mode at 260 cm⁻¹. In the M₁ stability region, below P_c, both modes are insensitive to hydrostatic compression (see Figs. 9(a) and 9(b)) and accurate wavenumbers measurements beyond the possible drifts of the equipment can be done using the B_g(2) mode as an internal reference. Above P_c, the A_g(4) scales linearly with *e*₃₃² (see Fig. 9(c)) or *e*_{Total}² (not shown) whereas the B_g(2) scales linearly with *e*₃₃⁴ or *e*_{Total}⁴.

The high-wavenumbers modes, B_g(4) at 340 cm⁻¹ (see Fig. S11) or B_g(8) at 665 cm⁻¹ (not shown), scale linearly with the monoclinic volume (M₁ or M₁') with no measurable discontinuity at P_c= 13.9(1) GPa. The A_g(9) mode at 615 cm⁻¹ and A_g(5)+B_g(5) doublet at 389/393 cm⁻¹ scale linearly with the octahedron volume (see Fig. S11(c-d)). The apparent discontinuity in the v(P) at P_c is due to the non-linear pressure dependence of the oxygen octahedron volume (see Fig. 3c).

Conclusion

The phase diagram of VO₂ has been investigated in the past but several aspects remained unclear. Indeed, the influence of non-hydrostatic components induced either by the pressure-transmitting medium or the form of the sample (powder vs single crystal) on the phase transition led to some discrepancies. Here, we present a combined X-ray diffraction and Raman spectroscopy investigations of high-quality VO₂ single crystal under pressure using Helium as the pressure transmitting medium. For the first time, a pressure-induced soft mode is observed. This behaviour is supposed to drive a transition towards a M₂ phase at pressure around 26 GPa. However, an intermediate phase transition is observed at 13.9 GPa, hindering this phonon instability. The isostructural nature of the phase transition at 13.9 GPa is confirmed experimentally. The microscopic mechanism is clarified and is based on the displacements of oxygen atoms. A phenomenological analysis based on the Landau theory of phase transition is proposed to describe the P-T phase diagram. Considering a strong anharmonic potential, the phase transitions, including the isostructural one, are described. The coupling with strains can explain the shift of the transition lines found in doped VO₂ or in thin films. At higher pressure, a phase transition to a metallic phase, probably triclinic, is observed starting from 32-35 GPa. On decompression, this phase transforms to another triclinic structure. Using high-pressure allows for separating overlapping peaks at ambient conditions and brings some new insights into the assignment of the different modes observed in Raman spectra. In addition, the results of the Raman spectroscopy allow relating some vibrational to different strain components or to pressure-induced microscopic variations such as the octahedron volume. This opens the opportunity to characterize the thin films in terms of structure, nature and amplitude of strain.

Acknowledgements

PB acknowledges the French CNRS for financial support through Tremplin@INP2020 and C. Goujon, C. Felix, Ch. Bouchard, A. Prat and J. Debray (CNRS, Institut Néel Grenoble) and J. Jacobs (ESRF Grenoble) for their technical help. The authors are grateful to ESRF ID15b for in-house beamtime allocation. Ch. Lepoittevin (UGA Institut Néel Grenoble) and W.A. Crichton (ESRF Grenoble) are also acknowledged for their advice on crystallographic questions. LB acknowledges the PROCOP Mobilität Programm for financing two months visit in Grenoble. LN2 is a joint International Research Laboratory (IRL 3463) funded and co-operated in Canada by Université de Sherbrooke (UdS) and in France by CNRS as well as ECL, INSA Lyon, and Université Grenoble Alpes (UGA). It is also supported by the Fonds de Recherche du Québec Nature et Technologie (FRQNT).

Annex 1

Although the active order parameter R_1^- is four-components [^{119,120}], only one single component is relevant to account for the rutile to M_1 structure distortion and becomes non-zero in the low-symmetry phase. This allows considering for R_1^- - M_1 an effective phenomenological model with one-component order parameter. The R_1^- symmetry forbids odd-degree terms in a free-energy expansion, and we get a canonical form for the Landau potential expanded to the tenth-degree:

$$F(\eta, P, T) = a_1(P, T) \eta^2 + a_2(P, T) \eta^4 + a_3 \eta^6 + a_4 \eta^8 + a_5 \eta^{10}. \quad (\text{A1})$$

The mathematical analysis of the model has been performed by Gufan [¹²⁰] who concluded that the minimal degree of $F(\eta)$ required to describe two consecutive first-order phase transitions (here, R- M_1 and M_1 - M_1') is ten (see also [¹⁰⁰] and references therein). This model allows to describe two low-symmetry phases. These phases have identical symmetries but differ by the magnitude of the order-parameter η . Therefore, the isostructural transition is intrinsically included into this description. Figure A1 shows the evolution of the theoretical phase diagram with increasing power of the free-energy F . Thus, for VO_2 undergoing two discontinuous phase transitions, R- M_1 and M_1 - M_1' (Fig.A1(c)), the phenomenological model (A1) is sufficient assuming $a_4 < 0$ and $a_5 > 0$, with M_1 - M_1' phase transition being iso-structural. Notice that to choose the maximal degree of expansion (between eight and ten) the main point is the character (continuous or discontinuous) of the first transition R- M_1 .

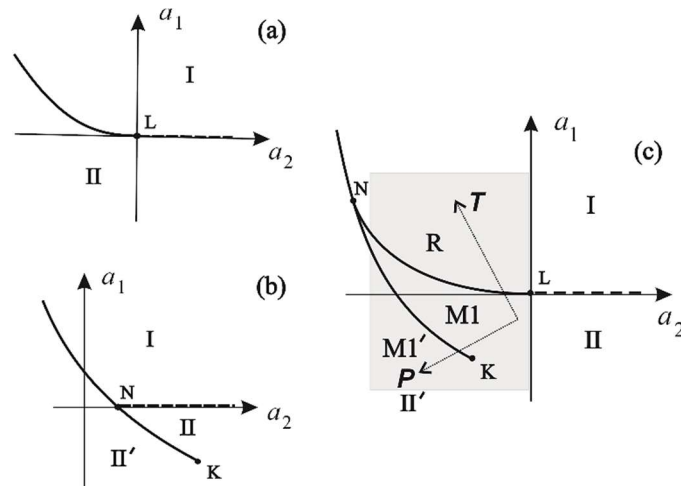


Figure A1. Equilibrium phase diagram corresponding to the free-energy (A1) in the plane of phenomenological coefficients (a_1, a_2) for: (a) canonical six-degree expansion ($a_3 > 0, a_4 = a_5 = 0$); (b) eight-degree potential ($a_3 < 0, a_4 > 0, a_5 = 0$); (c) ten-degree expansion ($a_3 < 0, a_4 < 0, a_5 > 0$). Figure (c) schematically shows “pressure (P)-temperature (T)” plane (grey area, dotted axes). Solid line – first-order, dashed – second-order phase transition lines. L – Landau tricritical point, N – triple point, K – critical end-point of the iso-structural phase transition.

Figure 1:

(color online) VO_2 monoclinic cell parameters with increasing pressure; (a) a_{M1} axis, (b) b_{M1} axis, (c) β angle between a_{M1} and c_{M1} , and (d) c_{M1} axis in the M_1 phase $P2_1/n$ cell choice 2. The full lines correspond to BM EoS between 0 and 34 GPa (see text). Insert in figure (a) shows the VV dimmers along the monoclinic a_{M1} axis. Insert in figure (b) shows the VO_6 octahedra in the (b_{M1}, c_{M1}) plane.

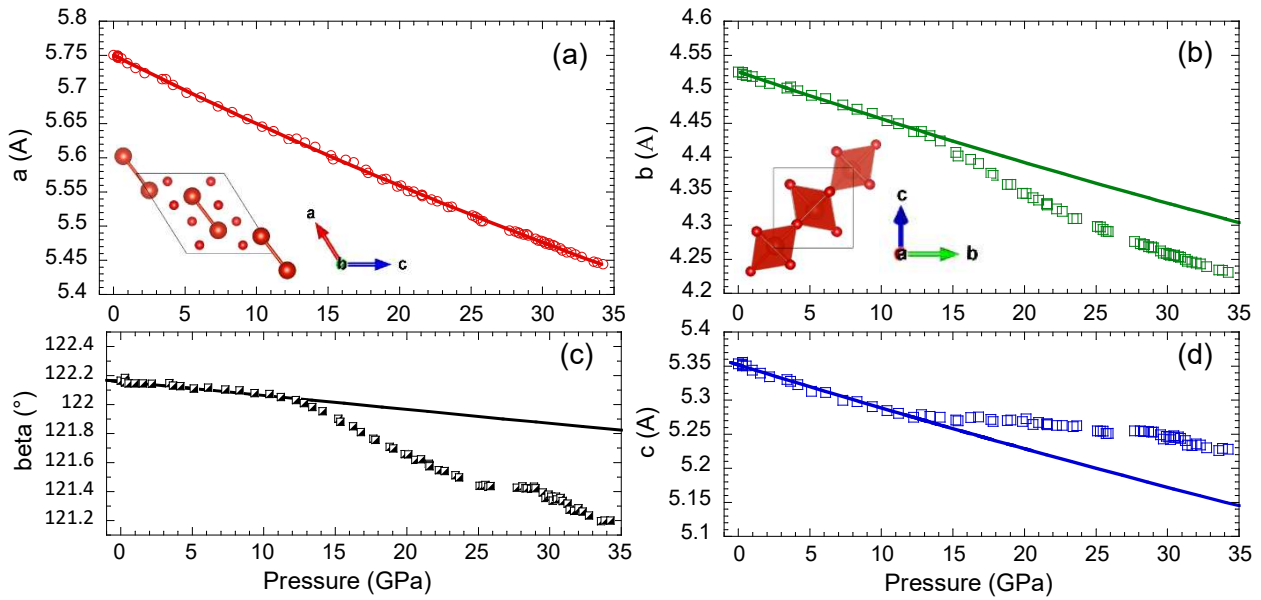


Figure 2:

(color online) Spontaneous deformations calculated in the high-pressure monoclinic cell against the original low pressure monoclinic M_1 using the EoS extrapolated above 14 GPa. The full lines are square root functions with $(P-P_c)$ with fixed $P_c=13.9$ GPa.

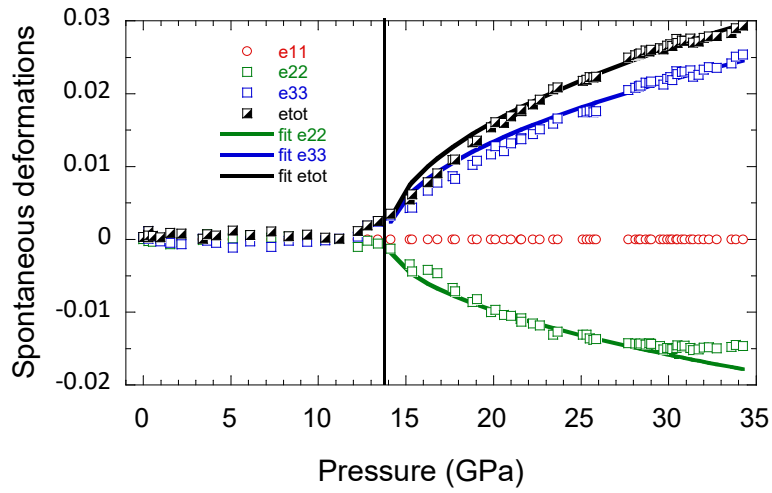


Figure 3:

(color online) VO₂ monoclinic parameters with increasing pressure (a) volume for Z=4 and F-f plot in the insert, (b) vanadium distances inside VV dimmers, (c) volume of VO₆ polyhedron. The full lines correspond to third order BM EoS. Others EoS from previous works are reported for comparison.

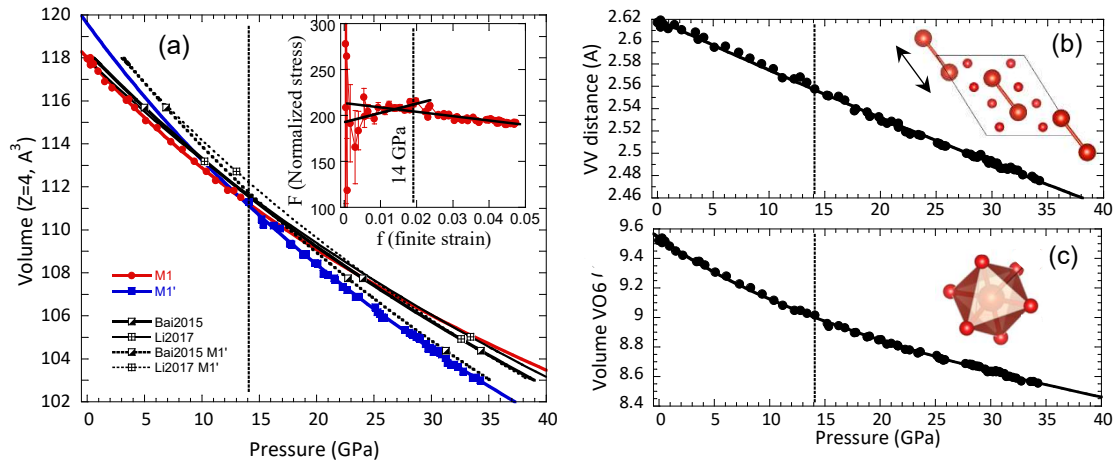


Figure 4:

(color online) Pressure dependence of (a) Vanadium fractional coordinates $V(x)+0.712$, $V(y)-0.478$ and $V(z)+0.473$ and (b) fractional oxygen displacements measured after subtracting the displacements extrapolated from the behavior below 14GPa in space-group $P2_1/n$ ($n^\circ 14$, $Z=4$, cell choice 2). The full lines in (b) are square root function with $(P- P_c)$ with fixed $P_c=13.9$ GPa.

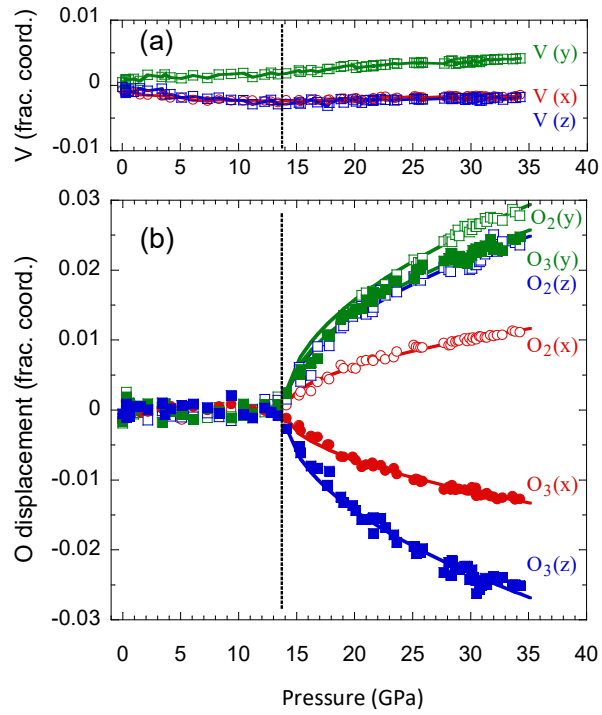


Figure 5:

(color online) Result of the LeBail profile fitting in the triclinic P-1 unit-cell at 35 GPa for phase X. Expected diffraction peaks are indicated by ticks. The difference between the experimental and the fit is reported at the bottom. Insert show the two-dimensional image of the crystal with tentative indexing.

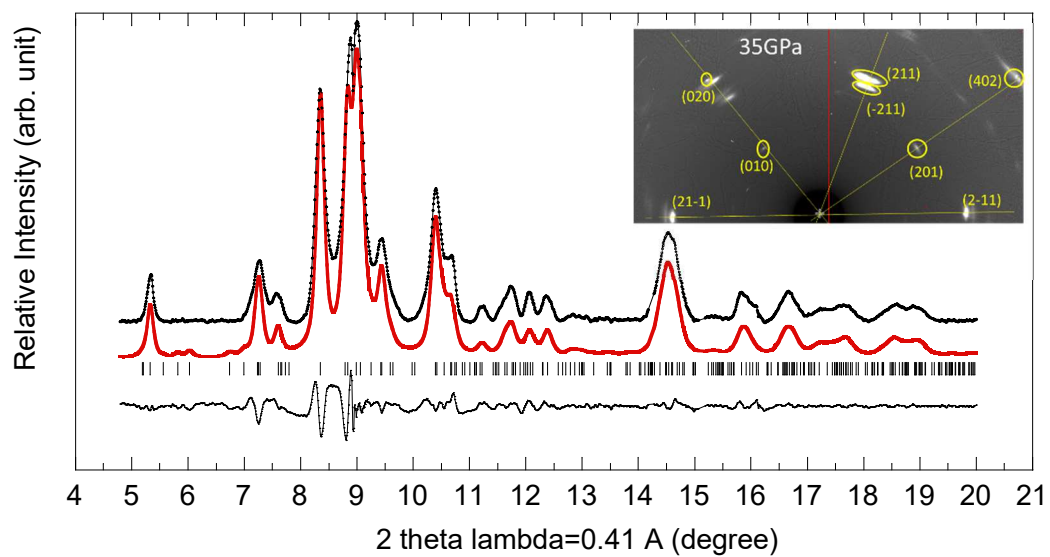


Figure 6:

(color online) Low wavenumber part (70-340 cm^{-1}) of the Raman spectra measured on VO_2 single crystal showing the softening/hardening of the 145 cm^{-1} Raman mode under increasing pressure. Pressures are quoted on the left of each spectrum. Black lines correspond to monoclinic M_1 phase. Red lines highlight the pressure higher than $P_c = 13.9(1)$ GPa. The symmetry A_g or B_g of each mode is indicated at the bottom.

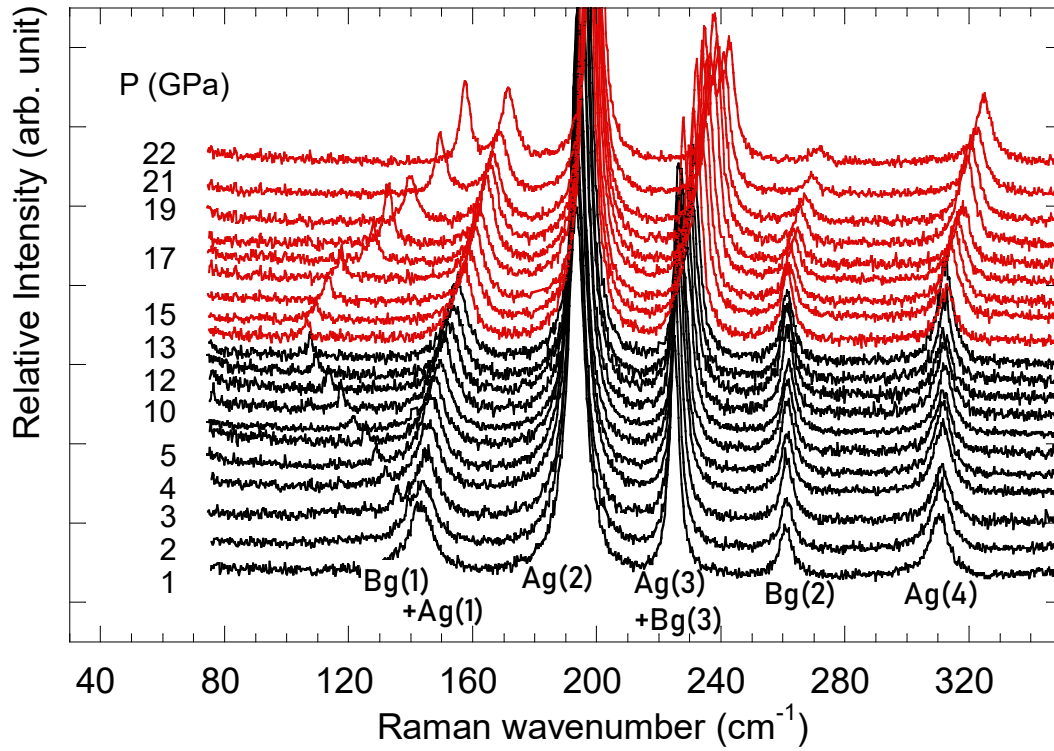


Figure 7:

(color online) Low wavenumber Raman spectral parameters measured under increasing hydrostatic pressure; (a) wavenumbers of the Ag(1), Bg(1), Ag(2), Ag(3) and Bg(3) modes (see labels in figure 6), (b) integrated intensity (area/s) of the Ag(1) and Bg(1) modes, (c) integrated intensity (area/s) of the most intense Ag(2) mode, (d) HWHM of the Ag(2) mode and of the Ruby pressure marker. Red and blue colours stand for Ag and Bg symmetry respectively.

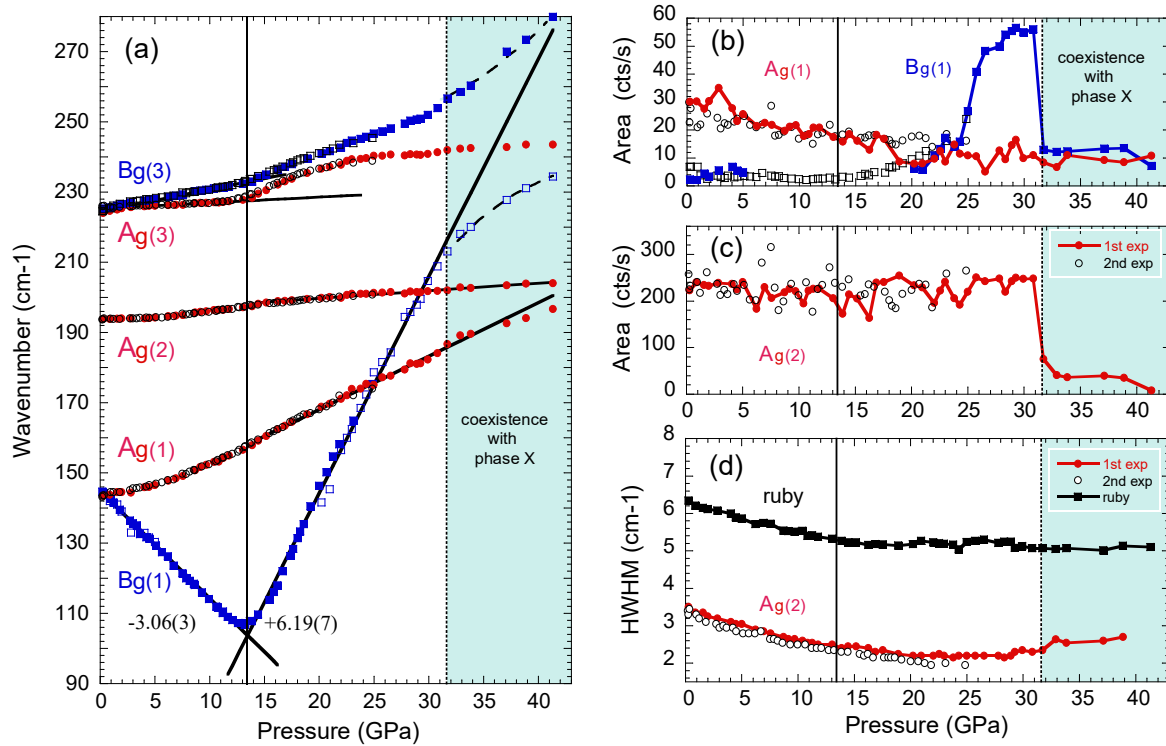


Figure 8:

(color online) Spontaneous Raman shift $w(M_1')-w(M_1)$ after subtracting the wavenumber $w(M_1)$ extrapolated above P_c from the behavior before $P_c=14$ GPa (a) Ag(3) and Bg(3) at 225 cm^{-1} against $|e_{22}|$ spontaneous strain along b_{M1} and (c) Bg(3) at 225 cm^{-1} against e_{33}^2 spontaneous strain along c_{M1} .

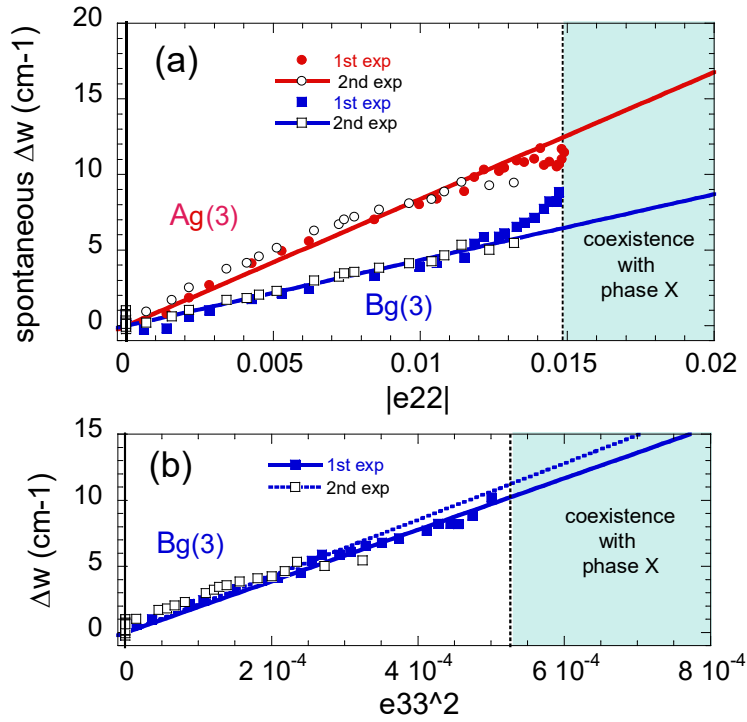


Figure 9:

(color online) Wavenumber of the Raman modes measured under increasing hydrostatic pressure on VO₂. (a) Bg(2) at 260cm⁻¹, and (b) Ag(4) at 310 cm⁻¹. The slopes dv/dP are reported in different pressure regions. (c) Ag(4) at 310 cm⁻¹ spontaneous Raman shift against e_{33}^2 spontaneous strain along c_{M1} .

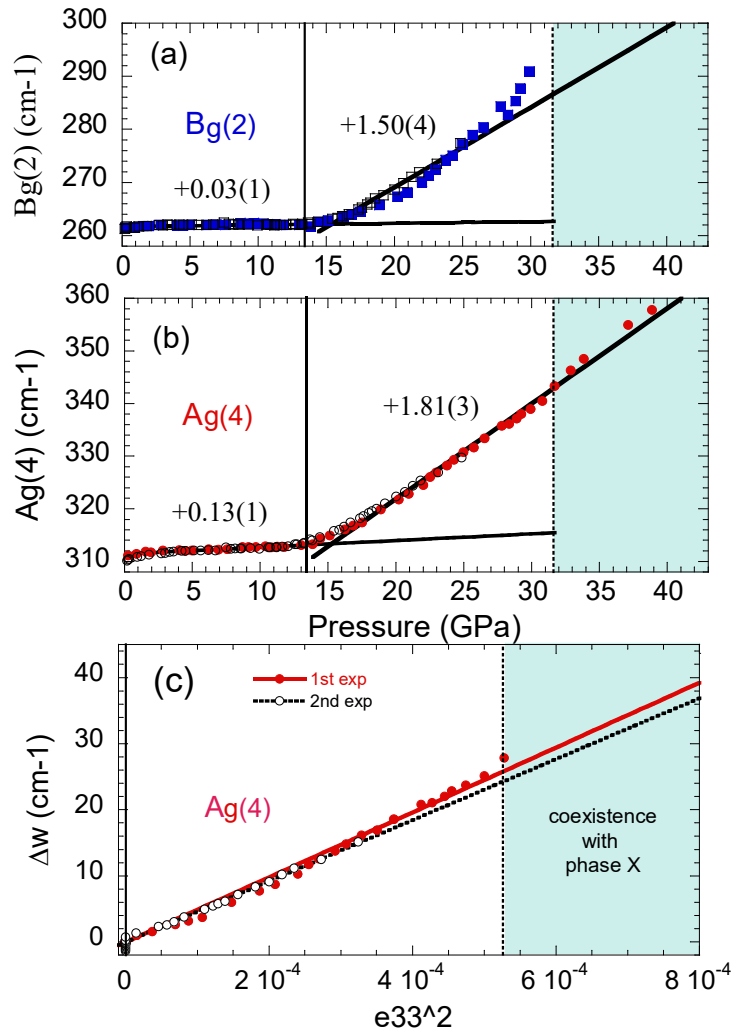


Figure 10:

(color online) Raman spectrum measured during decompression from 42 GPa. The signature of Phase X (in red at 28.7 GPa) is maintained up to 22 GPa and is transformed to a triclinic phase between 22 and 18.5 GPa. A coexistence between both structures is observed up to 3 GPa. A strained triclinic phase is retained at atmospheric pressure and room temperature. The spectra are corrected from a linear background.

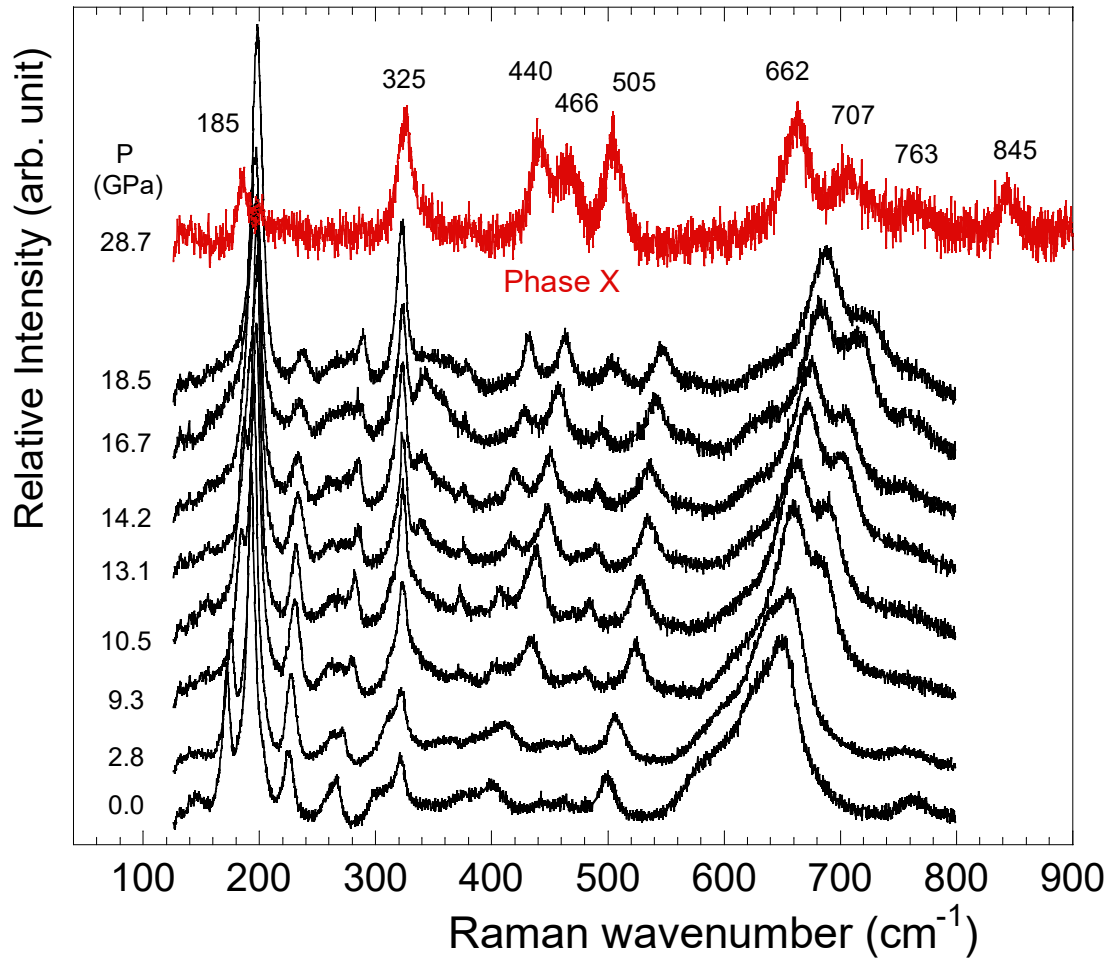


Figure 11:

Equilibrium phase diagram corresponding to the free-energy (3) in the plane of phenomenological coefficients (a_1, a_2) for $0 < a_2 < (c_{12}^2/4b_2)$, $c_{12} < 0$, $a_4 < 8b_2$, $a_5 > 0$. Solid line – first-order, dashed – second-order phase transition lines. K – critical end-point, N_1 and N_2 are three-phase points. Pressure (P) and temperature (T) axes are shown schematically.

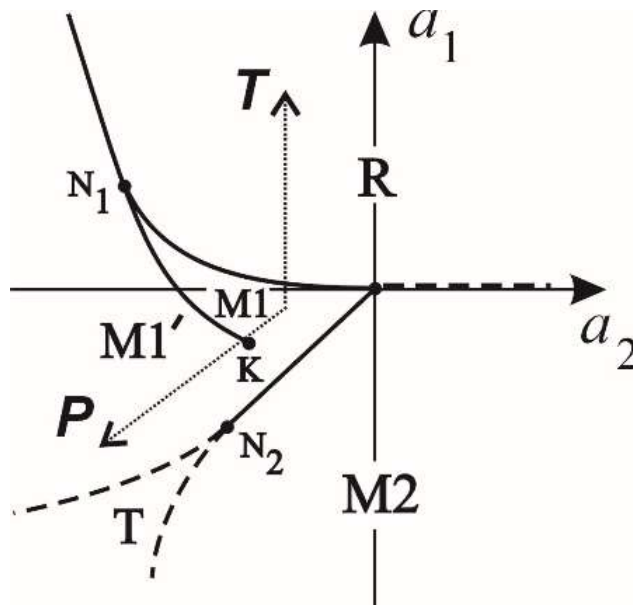


Figure A1:

Equilibrium phase diagram corresponding to the free-energy (2) in the plane of phenomenological coefficients (a_1, a_2) for: (a) canonical six-degree expansion ($a_3 > 0, a_4 = a_5 = 0$); (b) eight-degree potential ($a_3 < 0, a_4 > 0, a_5 = 0$); (c) ten-degree expansion ($a_3 < 0, a_4 < 0, a_5 > 0$). Figure (c) schematically shows “pressure (P)-temperature (T)” plane (grey area, dotted axes). Solid line – first-order, dashed – second-order phase transition lines. L – Landau tricritical point, N – triple point, K – critical end-point of the iso-structural phase transition.

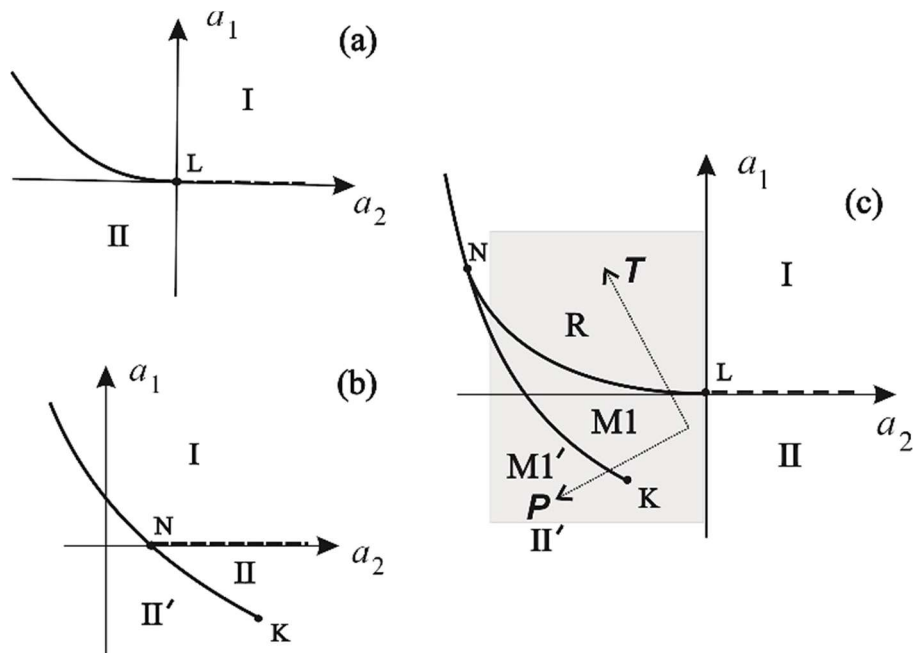


Table 1.

Position in wavenumber (cm^{-1}) of the Raman active modes measured experimentally or calculated for monoclinic M_1 phase of VO_2 and symmetry assignment propositions from literature. Lines in dark gray or light gray highlight the A_g or B_g symmetry of the Raman modes. The stars ***, **, * indicate the Raman intensity from most intense to less intense.

Position (cm^{-1})	[92]	[93]	[94]	[17]	[95]	[98] calc.	[96]	[97]	[99] calc.	Monoclinic M_1 This work
** 145	-	-	A_g	B_g	-	A_g	B_g	A_g+B_g	A_g	$A_g(1)+B_g(1)$
*** 190	A_g	A_g	A_g	A_g	A_g	A_g+B_g	A_g	A_g	A_g+B_g	$A_g(2)$
*** 225	A_g	A_g	A_g	A_g	A_g	A_g+B_g	A_g	A_g+B_g	A_g+B_g	$A_g(3)+B_g(3)$
* 260	A_g	B_g+B_g	B_g+B_g	-	-	B_g+B_g	B_g	B_g	B_g	$B_g(2)$
** 310	A_g	A_g	A_g	-	B_g	A_g	A_g	A_g	A_g	$A_g(4)$
340	A_g	B_g	B_g	-	A_g	A_g	A_g	A_g	A_g+B_g	$B_g(4)$
** 390	A_g	A_g	A_g	-	A_g	A_g	A_g	A_g	A_g	$A_g(5)$
** 394	-	B_g	B_g	-	-	B_g	B_g	B_g	-	$B_g(5)$
440	A_g	B_g	B_g	-	-	B_g	B_g	B_g	B_g	$A_g(6)$
445	-	B_g	A_g	-	-	B_g	B_g	-	B_g	$B_g(6)$
485	-	B_g	B_g	-	-	B_g	B_g	B_g	B_g	$B_g(7)$
500	A_g	A_g	A_g	-	A_g	A_g	A_g	A_g	A_g	$A_g(7)$
** 595	B_g	A_g	A_g	-	-	B_g	A_g	B_g	B_g	$A_g(8)$
*** 615	A_g	A_g	A_g	-	A_g	A_g	A_g	A_g	A_g	$A_g(9)$
665	-	B_g	B_g	-	-	A_g	B_g	A_g	A_g	$B_g(8)$
850	-	B_g	B_g	-	-	B_g	B_g	B_g	B_g	$B_g(9)$

Table 2:

(color online) Wavenumber dependence with pressure for Raman modes in M_1 and M_1' high pressure monoclinic VO_2 . SM= Soft mode. Bg modes in green. Grüneisen parameter $\gamma=(K/v) \cdot (dv/dP)_T$. Errors are in parenthesis.

Raman mode Symmetry	Position @00GPa (cm^{-1})	Slope ($\text{cm}^{-1}/\text{GPa}$)	Grüneisen γ	Position @13.9GPa (cm^{-1})	Slope ($\text{cm}^{-1}/\text{GPa}$)
Ag(1)	142.9(2)	+0.77(4)	+1.04(9)	158.9(3)	+1.52(2)
Bg(1)	144.9(2)	-3.06(3)	-4.1(2)	106.4(7)	+6.19(7)
Ag(2)	192.5(1)	+0.36(1)	+0.36(2)	198.5(1)	+0.22(1)
Bg(3)	224.6(2)	+0.62(2)	+0.53(4)	233.6(1)	+1.15(1)
Ag(3)	225.4(1)	+0.16(1)	+0.14(1)	229.3(2)	+1.10(4)
Bg(2)	261.7(1)	+0.03(1)	+0.022(8)	259.9(2)	+1.50(4)
Ag(4)	311.4(1)	+0.13(1)	+0.081(9)	311(4)	+1.81(3)
Bg(4)	340.7(3)	+4.42(4)	+2.52(11)	400.1(4)	+4.06(4)
Ag(5)	388.8(3)	+4.06(4)	+2.03(9)	444.1(3)	+2.79(3)
Bg(5)	392.8(5)	+4.32(6)	+2.13(10)	450.7(3)	+2.61(3)
Bg(6)	442	----	----	----	----
Ag(6)	442.8(3)	+2.35(4)	+1.03(5)	477(1)	+3.15(9)
Bg(7)	483	----	----	----	----
Ag(7)	499.3(1)	+2.64(1)	+1.03(4)	536.2(2)	+2.02(2)
Ag(8)	594.5(8)	+4.37(11)	+1.43(8)	654.5(6)	+2.78(12)
Ag(9)	613.4(2)	+3.86(2)	+1.22(5)	668.8(3)	+2.37(3)
Bg(8)	662.8(7)	+2.85(9)	+0.83(5)	703.8	+2.72(7)
Bg(9)	----	----	----	----	----

Bibliography

- ¹ - F.J.Morin, Phys. Rev. Letters 3 (1959) 34-36.
- ² - K.Liu, S.Lee, S.Yang, O.Delaire, J.Wu, Materials Today 21 (2018) 875-896.
- ³ - Y.Ke, S.Wang, G.Liu, M.Li, T.J.White, Y.Long, Small 14 (2018) 1802025 p1-29.
- ⁴ - R.Shi, N.Shen, J.Wang, W.Wang, A.Amini, N.Wang, C.Cheng, Appl. Phys. Rev. 6 (2019) 011312 1-26.
- ⁵ - W.H.Brito, M.C.O.Aguiar, K.Haule, G.Kotliar, Phys. Rev. Letters 117 (2016) 056402.
- ⁶ - W.R.Mondal, E.Evlyukhin, S.A. Howard, G.J. Paez , H.Paik, D.G.Schlom, L.F.J.Piper ,W.-C.Lee, Phys. Rev. B 103 (2021) 214107.
- ⁷ - J.B.Goodenough, J. Solid State Chem. 3 (1971) 490-500.
- ⁸ - C.J.Hearn, J.Phys.C: Solid State Phys. 5 (1972) 1317-1334.
- ⁹ - A.Zylbersztejn, N.F.Mott, Phys. Rev. B 11 (1975) 4383-4395.
- ¹⁰ - D.Paquet, P. Leroux-Hugon, Phys. Rev. B, 22 (1980) 5284-5301.
- ¹¹ - F.Gervais, W.Kress, Phys. Rev. B 31 (1985) 4809-4814.
- ¹² - S.Shin, S.Suga, M.Taniguchi, M.Fujisawa, H.Kanzaki, A.Fujimori, H.Daimon, Y.Ueda, K.Kosuge, S.Kachi, Phys. Rev. B 41 (1990) 4993-5009.
- ¹³ - R.R.Andronenko, I.N.Goncharuk, V.Yu.Davydov, F.A.Chudnovskii, E.B.Shadrin, Phys. Solid State 36 (1994) 1136-1139.
- ¹⁴ - R.M. Wentzcovitch, W.W.Schulz, Ph.B.Allen, Phys.Rev. Letters 72 (1994) 3389-3392.
- ¹⁵ - T.M.Rice, H.Launois, J.P.Pouget, Phys. Rev. Letters 73 (1994) 3042.
- ¹⁶ - V.Eyert, Ann. Phys. 11 (2002) 650-702.
- ¹⁷ - A.Cavalleri, Th.Dekorsy, H.H.W.Chong, J.C.Kieffer, R.W.Schoenlein, Phys. Rev. B 70 (2004) 161102(R).
- ¹⁸ - M.M.Qazilbash, M.Brehm, B.-G.Chae, P.-C.Ho, G.O.Andreev, B.-J.Kim, S.J.Yun, A.V.Balatsky, M.B.Maple, F.Keilmann, H.-T.Kim, D.N.Basov, Science 318 (2007) 1750-1753.
- ¹⁹ - M.Netsianda, P.E.Ngoepe, C.R.A.Catlow, S.M.Woodley, Chem. Mater. 20 (2008) 1764-1772.
- ²⁰ - S.M.Woodley, Chemical Physics Letters 453 (2008) 167-172.
- ²¹ - B.Lazarovits, K.Kim, K.Haule, G.Kotliar, Phys. Rev. B 81 (2010) 115117.
- ²² - V.Eyert, Phys. Rev. Letters 107 (2011) 016401.
- ²³ - X.Yuan, Y.Zhang, T.A.Abtew, P.Zhang, W.Zhang, Phys. Rev. B 86 (2012) 235103.
- ²⁴ - S.Kim, K.Kim, C.-J. Kang, B.I. Min, Phys. Rev. B 87 (2013) 195106.
- ²⁵ - J.D.Budai, J.Hong, M.E.Manley, E.D.Specht, C.W.Li, J.Z.Tischler, D.L.Abernathy, A.H.Said, B.M.Leu, L.A.Boatner, R.J.McQueeney, O.Delaire, Nature 515 (2014) 535-539.
- ²⁶ - I.-H.Hwang, Z.Jin, C.-I.Park, S.-W.Han, Scientific Reports 7 (2017) 14802.
- ²⁷ - T.V.Slusar, J.-C.Cho, H.-R.Lee, J.-W.Kim, S.J.Yoo, J.-Y.Bigot, K.-J.Yee, H.-T.Kim, Scientific reports 7 (2017) 16038.
- ²⁸ - T.J. Huffman, C. Hendriks, E.J. Walter, J. Yoon, H. Ju, R. Smith, G.L. Carr, H. Krakauer, M.M. Qazilbash, Phys. Rev. B 95 (2017) 075125, 1-6.
- ²⁹ - S.Lee, K.Hippalgaonkar, F.Yang, J.Hong, C.Ko, J.Suh, K.Liu, K.Wang, J.J.Urban, X.Zhang, C.Dames, S.A.Hartnoll, O.Delaire, J.Wu, Science 355 (2017) 371-374.
- ³⁰ - S.S.Majid, D.K.Shukla, F.Rahman, S.Khan, K.Gautam, A.Ahad, S.Francoual, R.J.Choudhary, V.G.Sathe, J.Strempfer, Phys. Rev. B 98 (2018) 075152.
- ³¹ - T.A.Mellan, H.Wang, U.Schwingenschlögl, R. Grau-Crespo, Phys. Rev. B 99 (2019) 064113.
- ³² - F.Grandi, A.Amaricci, M.Fabrizio, Phys. Rev. Research 2 (2020) 013298.
- ³³ - S.R.Sahu, S.S.Majid, A.Ahad, A.Tripathy, K.Dey, S.Pal, B.K.De, W.-P.Hsieh, R.Rawat, V.G.Sathe, D.K.Shukla, Phys. Rev. B 107 (2023) 134106.
- ³⁴ - D.B.McWhan, M.Marezio, J.P.Remeika, P.D.Dernier, Phys. Rev. B 10 (1974) 490-495.
- ³⁵ - J. Longo, P. Kierkegaard, Acta Chemica Scandinavica, 24 (1970) 420-426.
- ³⁶ - J.R.Brews, Phys. Review B 1 n°6 (1970) 2557-2568.
- ³⁷ - H. Terauchi, J.B. Cohen, Phys. Rev. B, 17 (1978) 2494-2496.
- ³⁸ - Y.M.Gufan, V.P.Popov, Sov. Phys. Crystallogr. 25 (1980) 527-532.
- ³⁹ - Y.M.Gufan, V.P.Dmitriev, S.Rochal, Y.Cherner, Sov. Phys.:Solid State, 27 (1985) 1046.
- ⁴⁰ - Y.Gu, J.Cao, J.Wu, L.-Q.Chen, J. Applied Physics 108 (2010) 083517.
- ⁴¹ - J.Cao, Y.Gu, W.Fan, L.Q.Chen, D.F.Ogletree, K.Chen, N.Tamura, M.Kunz, C.Barret, J.Seidel, J.Wu, Nano Letters 10 (2010) 2667-2673.
- ⁴² - A.Tselev, E.Strelcov, I.A.Luk'yanchuk, J.D.Budai, J.Z.Tischler, I.N.Ivanov, K.Jones, R.Proksch, S.V.Kalinin, A.Kolmakov, Nanoletters 10 (2010) 2003-2011.

-
- ⁴³ - A.Tselev, I.A.Luk'yanchuk, I.N.Ivanov, J.D.Budai, J.Z.Tischler, E.Strelcov, A.Kolmakov, S.V.Kalinin, *Nanoletters* 10 (2010) 4409-4416.
- ⁴⁴ - W.Fan, J.Cao, J.Seidel, Y.Gu, J.W.Yim, C.Barrett, K.M.Yu, J.Ji, R.Ramesh, L.Q.Chen, J.Wu, *Phys. Rev. B* 83 (2011) 235102.
- ⁴⁵ - E.Strelcov, A.Tselev, I.Ivanov, J.D.Budai, J.Zhang, J.Z.Tischler, I.Kravchenko, S.V.Kalinin, A.Kolmakov, *Nanoletters* 12 (2012) 6198-6205.
- ⁴⁶ - N.F.Quackenbush, H.Paik, M.J.Wahila, S.Sallis, M.E.Holtz, X.Huang, A.Ganose, B.J.Morgan, D.O.Scanlon, Y.Gu, F.Xue, L.-Q.Chen, G.E.Sterbinsky, C.Schlueter, T.-L.Lee, J.C.Woicik, J.-H.Guo, J.D.Brock, D.A.Muller, D.A.Arena, D.G.Schlom, L.F.J.Piper, *Phys Rev B* 94 (2016) 085105.
- ⁴⁷ - J.P. Pouget, *Comptes rendus Physique*, 22 n°1 (2021) 37-87.
- ⁴⁸ - M.Marezio, D.B.McWhan, J.P.Remeika, P.D.Dernier, *Phys. Rev. B*, 5 (1972) 2542-2551.
- ⁴⁹ - B.L. Chamberland, *J. Solid State Chemistry* 7 (1973) 377-384.
- ⁵⁰ - J.P.Pouget, H.Launois, T.M.Rice, P.Dernier, A.Gossard, G.Villeneuve, P.Hagenmuller, *Phys Rev B* 10 (1974) 1801-1815.
- ⁵¹ - J.P.Pouget, H.Launois, *Journal de Physique Colloques* 37 (1976) C4-49-C4-57.
- ⁵² - M.Ghedira, H.Vincent, M.Marezio, J.C.Launay, *J. Solid State Chem.* 22 (1977) 423-438.
- ⁵³ - J.P.Pouget, H.Launois, J.P. D'Haenens, P.Merenda, T.M.Rice, *Phys. Rev. Letters* 35 (1975) 873-875.
- ⁵⁴ - J.Galy, G.Miehe, *Solid State Science* 1 (1999) 433-448.
- ⁵⁵ - A.C.Jones, S.Berweger, J.Weil, D.Cobden, M.B.Raschke, *Nano Letters* 10, (2010) 1574-1581.
- ⁵⁶ - H.Guo, K.Chen, Y.Oh, K.Wang, C.Dejoie, S.A.Syed Asif, O.L.Warren, Z.W.Shan, J.Wu, A.M.Minor, *Nanoletters* 11 (2011) 3207-3213.
- ⁵⁷ - J.M. Atkin, S. Berweger, E.K. Chavez, M.B. Raschke, J. Cao, W. Fan, J. Wu, *Phys. Rev. B* 85 (2012) 020101(R).
- ⁵⁸ - J.H.Park, J.M.Coy, T.S.Kasirga, C.Huang, Z.Fei, S.Hunter, D.H.Cobden, *Nature* 500 (2013) 431-434.
- ⁵⁹ - J.D.Budai, A.Tselev, J.Z.Tischler, E.Strelcov, A.Kolmakov, W.J.Liu, A.Gupta, J.Narayan, *Acta Materialia* 61 (2013) 2751-2762.
- ⁶⁰ - M.Liu, A.J.Sternbach, M.Wagner, T.V.Sluser, T.Kong, S.L.Bud'ko, S.Kittiwatanakul, M.M.Qazilbash, A.McLeod, Z.Fei, E.Abreu, J.Zhang, M.Goldflam, S.Dai, G.-X.Ni, J.Lu, H.A.Bechtel, M.C.Martin, M.B.Raschke, R.D.Averitt, S.A.Wolf, H.-T.Kim, P.C.Canfield, D.N.Basov, *Phys. Rev. B* 91 (2015) 245155.
- ⁶¹ - H.Kim, T.V.Sluser, D.Wulferding, I.Yang, J.-C.Cho, M.Lee, H.C.Choi, Y.H.Jeong, H.-T.Kim, J.Kim, *Applied Physics Letters* 109 (2016) 233104.
- ⁶² - M.Liu, S.Xie, L.Weil, M.Galluzzi, Y.Li, Q.Wang, X.Zhou, Y.Wang, J.Li, *Acta Materialia* 195 (2020) 720-727.
- ⁶³ - J.Cao, E.Ertekin, V.Srinivasan, W.Fan, S.Huang, H.Zheng, J.W.L.Yim, D.R.Khanal, D.F.Ogletree, J.C.Grossman, J.Wu, *Nature Nanotechnology* 4 (2009) 732-737.
- ⁶⁴ - N.B.Aetukuri, A.X.Gray, M.Drouard, M.Cossale, L.Gao, A.H.Reid, R.Kukreja, H.Ohldag, C.A.Jenkins, E.Arenholz, K.P.Roche, H.A.Dürr, M.G.Samant, S.S.P.Parkin, *Nature Physics* 9 (2013) 661-666.
- ⁶⁵ - S. Kittiwatanakul, S.A.Wolf, J.Lu, *Applied Physics Letters* 105 (2014) 073112.
- ⁶⁶ - E.Arcangeletti, L.Baldassarre, D.DiCastro, S.Lupi, L.Malavasi, C.Marini, A.Perucchi, P. Postorino, *Phys Rev Letters* 98 (2007) 196406.
- ⁶⁷ - C.Marini, E.Arcangeletti, D.DiCastro, L.Baldassarre, A.Perucchi, S.Lupi, L.Malavasi, L.Boeri, E.Pomjakushina, K.Conder, P.Postorino, *Phys. Rev. B* 77, 235111 (2008).
- ⁶⁸ - C.Marini, L.Baldassarre, M.Baldini, A.Perucchi, D.DiCastro, L.Malavasi, S.Lupi, P. Postorino, *High Pressure Research* 30, (2010) 55-59.
- ⁶⁹ - H.Zhang, Q.Li, B.Cheng, Z.Guan, R.Liu, B.Liu, Z.Liu, X.Li, T.Cui, B.Liu, *RSC Advances* 6 (2016) 104949.
- ⁷⁰ - X.Zhang, J.Zhang, F.Ke, G.Li, Y.Ma, X.Liu, C.Liu, Y.Han, Y.Ma, C.Gao, *RSC Advances* 5 (2015) 54843.
- ⁷¹ - L.Bai, Q.Li, S.A.Corr, Y.Meng, C.Park, S.V.Sinogeikin, C.Ko, J.Wu, G.Shen, *Phys. Rev. B* 91, 104110 (2015).
- ⁷² - M.Mitrano, B.Maroni, C.Marini, M.Hanfland, B.Joseph, P.Postorino, L.Malavasi, *Phys. Rev. B* 85, 184108 (2012).
- ⁷³ - V.Balédent, T.T.F.Cerqueira, R.Sarmiento-Pérez, A.Shukla, Ch.Bellin, M.Marsi, J.-P.Itié, M.Gatti, M.A.L.Marques, S.Botti, J.-P. Rueff, *Phys. Rev. B* 97, 024107 (2018).
- ⁷⁴ - Q.Li, H.Zhang, C.Lin, F.Tian, J.S. Smith, C.Park, B.Liu, G.Shen, *J. Alloys and Compounds* 709 (2017) 260-266.
- ⁷⁵ - M.Baldini, P.Postorino, L.Malavasi, C.Marini, K.W.Chapman, H.-K. Mao, *Phys. Rev. B* 93, 245137 (2016).
- ⁷⁶ - H.He, H.Gao, W.Wu, S.Cao, J.Hong, D.Yu, G.Deng, Y.Gao, P.Zhang, H.Luo, W.Ren, *Phys. Rev. B* 94, 205127 (2016).
- ⁷⁷ - H.Zhang, Q.Li, F.Wang, R.Liu, Y.Mao, Z.Liu, X.Li, K.Yang, T.Cui, B.Liu, *J. Phys. Chem. C* 123 (2019) 955-962.
- ⁷⁸ - S.-Y.Xie, L.Wang, F.Liu, X.-B.Li, L.Bai, V.B.Prakapenka, Z.Cai, H.-k.Mao, S.Zhang, H.Liu, *J. Phys. Chem. Lett.*, 9 (2018) 2388-2393.

-
- ⁷⁹ - H.Zhang, Z.Guan, B.Cheng, Q.Li, R.Liu, J. Zhang, Z.Liu, K. Yang, T.Cui, B.Liu, RSC Advances 7 (2017) 31597.
- ⁸⁰ - Y.Chen, S.Zhang, F.Ke, C.Ko, S.Lee, K.Liu, B.Chen, J.W.Ager, R.Jeanloz, V.Eyert, J.Wu, nano Lett. 17 (2017) 2512-2516.
- ⁸¹ - Y. Bando, M. Kyoto, T. Takada, S. Muranaka, J. Crystal Growth, 45 (1978) 20-24.
- ⁸² - Holzapfel, W. B., Journal of applied Physics 93 (2003) 1813-1818.
- ⁸³ - K.Takemura, J. Applied Physics, 89 (2001) 662-668.
- ⁸⁴ - A.Dewaele, P.Loubeyre, High Pressure Research 27 (2007) 419-429.
- ⁸⁵ - A.Dewaele, P.Loubeyre, M.Mezouar, Phys. Rev. B 70 (2004) 094112.
- ⁸⁶ - C.Prescher, V.B.Prakapenka, High Pressure Res. 35(3) (2015) 223-230.
- ⁸⁷ - M.Wojdyr, Journal of applied crystallography 43 (2010) 1126-1128.
- ⁸⁸ - CrysAlisPRO, Oxford Diffraction /Agilent Technologies UK Ltd, Yarnton, England.
- ⁸⁹ - V.Petricek, M.Dusek, L.Palatinus, Zeitschrift fur Kristallographie 229(5) (2014) 345-352.
- ⁹⁰ - K.Momma, F.Izumi, J. Appl. Crystallogr. 44 (6) (2011),1272-1276.
- ⁹¹ - J. Rodriguez-Carvajal, Physica B 192 (1993), 55-69.
- ⁹² - A.G.Aronov, D.N.Mirlin, I.I.Reshina, F.A.Chudnovskii, Sov. Phys. Solid State 19 (1977) 110-114.
- ⁹³ - P. Schilbe, Physica B, 316-317 (2002) 600-602.
- ⁹⁴ - P. Schilbe, D.Maurer, Materials Science Engineering A 370 (2004) 449-452.
- ⁹⁵ - J.Y. Chou, J.L. Lensch-Falk, E.R. Hemesath, L.J. Lauhon, J. Applied Phys. 105 (2009) 034310.
- ⁹⁶ - M. Zaghrioui, J.Sakai, N.H.Azhan, K.Su, K.Okimura, Vibrational Spectroscopy 80 (2015) 79-85.
- ⁹⁷ - K.Shibuya, A.Sawa, J. Applied Phys. 122 (2017) 015307.
- ⁹⁸ - X. Yuan, W. Zhang, P. Zhang, Phys. Rev. B 88 (2013) 035119.
- ⁹⁹ - R.Basu, A.Patsha, S.Chandra, S. Amirthapandian, R.K.Gururaj, A.Dasgupta, S.Dhara, J. Phys. Chem. C, 123 (2019) 11189-11196.
- ¹⁰⁰ - V.Dmitriev, *Discontinuous Phase Transitions in Condensed Matter* (World Scientific, Singapore, 2023).
- ¹⁰¹ - H.-T.Kim, Y.W.Lee, B.-J.Kim, B.-G.Chae, S.J.Yun, K.-Y.Kang, K.-J.Han, K.-J.Yee, Y.S.Lim, Phys. Rev. Letters 97 (2006) 266401.
- ¹⁰² - Z.Tao, Tzong-Ru.T.Han, S.D.Mahanti, P.M.Duxbury, F.Yuan, C.-Y.Ruan, K.Wang, J.Wu, Phys. Rev. Letters 109 (2012) 166406.
- ¹⁰³ - J. Laverock, S. Kittiwatanakul, A.A. Zakharov, Y.R. Niu, B. Chen, S.A. Wolf, J.W. Lu, K.E. Smith, Phys. Rev. Letters 113 (2014) 216402.
- ¹⁰⁴ - D.Lee, B.Chung, Y.Shi, G.-Y.Kim, N.Campbell, F.Xue, K.Song, S.-Y.Choi, J.P.Podkaminer, T.H.Kim, P.J.Ryan, J.-W.Kim, T.R.Paudel, J.-H. Kang, J.W.Spinuzzi, D.A.Tenne, E.Y.Tsymbal, M.S.Rzchowski, L.Q.Chen, J. Lee, C.B.Eom, Science 362 (2018) 1037-1040.
- ¹⁰⁵ - S.Zhang, J.Y.Chou, L.Lauhon, Nano Letters 9 (2009) 4527-4532.
- ¹⁰⁶ - S.-J. Chang, W.-K. Hong, H.J. Kim, J.B. Lee, J. Yoon, H.C. Ko, Y.S. Huh, Nanotechnology 24 (2013) 345701.
- ¹⁰⁷ - S.-J. Chang, J.B.Park, G.Lee, H.J.Kim, J.-B.Lee, T.-S.Bae, Y.-K.Han, T.J.Park, Y.S.Huh, W.-K.Hong, Nanoscale 6 (2014) 8068.
- ¹⁰⁸ - K.Okimura, N.H.Ashan, T.Hajiri, S.-I.Kimura, M.Zaghrioui, J.Sakai, J. Applied Physics 115 (2014) 153501.
- ¹⁰⁹ - E. Evlyukhin, S.A.Howard, H.Paik, G.J.Paez, D.J.Gosztola, C.N.Singh, D.G.Schlom, W.-C.Lee, L.F.J.Piper, nanoscale, 12 (2020) 18857.
- ¹¹⁰ - R.Srivastava, L.L.Chase, Phys. Rev. Letters 27 (1971) 727-730.
- ¹¹¹ - B.Y. Qu, H.Y. He, B.C. Pan, J. Applied Physics 110 (2011) 113517.
- ¹¹² - S.Wall, S.Yang, L.Vidas, M.Chollet, J.M.Glownia, M.Kozina, T.Katayama, T.Henighan, M.Jiang, T.A.Miller, D.A.Reis, L.A. Boatner, O.Delaire, M.Trigo, Science 362 (2018) 572-576.
- ¹¹³ - C.W.Rischau, X.He, G.Mazza, S.Gariglio, J.-M.Triscione, Ph.Ghosez, J.del Valle, Phys. Rev. B 107 (2023) 115139.
- ¹¹⁴ - E.Strelcov, A.Ievlev, A.Belianinov, A.Tselev, A.Kolmakov, S.V.Kalinin, Scientific Reports 6 (2016) 29216.
- ¹¹⁵ - P.Shvets, O.Dikaya, K.Maksimova, A.Goikhman, J. Raman Spectrosc. 50 (2019) 1226-1244.
- ¹¹⁶ - R.Basu, V.Srihari, M.Sardar, S. K.Srivastava, S.Bera, S.Dhara, Scientific Report, 10 (2020) 1977.
- ¹¹⁷ - P.Shvets, K.Maksimova, A.Goikhman, J. Appl. Phys. 129 (2021) 055302.
- ¹¹⁸ - J.Li, L.Wu, S.Yang, X.Jin, W.Wang, J.Tao, L.Boatner, M.Babzien, M.Fedurin, M.Palmer, W.Yin, O.Delaire, Y.Zhu, Phys. Rev. X 12 (2022) 021032.
- ¹¹⁹ - Y.M.Gufan, V.P.Dmitiev, Sov. Phys. Crystallogr. 25 (1980) 6-10.
- ¹²⁰ - Y. M. Gufan, *Structural Phase Transitions* (Nauka, Moscow, 1982).